Ammonia and methane dairy emission plumes in the San Joaquin Valley of California from individual feedlot to regional scales

David J. Miller[1,2], Kang Sun[1], Lei Tao[1], Mark A. Zondlo[1], John B. Nowak[3,4], Zhen Liu[5], Glenn Diskin[6], Glen Sachse[7], Andreas Beyersdorf[6], Richard Ferrare[6] and Amy Jo Scarino[6,8]

Corresponding author: Mark A. Zondlo, Department of Civil and Environmental Engineering, Princeton University, Engineering Quadrangle E209A, 59 Olden Street, Princeton, NJ 08544, USA. (mzondlo@princeton.edu)

[1]Department of Civil and Environmental

Abstract. Agricultural ammonia (NH_3) emissions are highly uncertain, with high spatio-temporal variability and a lack of widespread in-situ mea-

Engineering, Princeton University,
Princeton, New Jersey, USA.

[2]now at: Institute at Brown for Environment and Society, Brown University, Providence, Rhode Island, USA.

[3]Cooperative Institute for Research in Environmental Sciences, U.C. Boulder, Boulder, Colorado, USA.

[4]now at: Aerodyne Research, Inc., Billerica, Massachusetts, USA.

[5]Combustion Research Facility, Sandia National Laboratories, Livermore, California, USA.

[6]NASA Langley Research Center, Hampton, Virginia, USA.

[7]National Institute of Aerospace, Hampton, Virginia, USA.

[8]Science Systems and Applications, Inc., Hampton, Virginia, USA.

surements. Regional NH_3 emission estimates with mass-balance or emission ratio approaches are uncertain due to variable NH_3 sources and sinks as well as unknown plume correlations with other dairy source tracers. We characterize the spatial distributions of NH_3 and methane (CH_4) dairy plumes using in-situ surface and airborne measurements in the Tulare dairy feedlot region of the San Joaquin Valley, California during the NASA DISCOVER-AQ 2013 field campaign. ***Surface NH_3 and CH_4 mixing ratios exhibit large variability with maxima localized downwind of individual dairy feedlots. The geometric mean NH_3:CH_4 enhancement ratio derived from surface measurements is 0.15 $\pm$ 0.03 ppmv ppmv^{-1}. Individual dairy feedlots with spatially distinct NH_3 and CH_4 source pathways led to statistically significant correlations between NH_3 and CH_4 in only 68% of the 69 downwind plumes sampled. At longer sampling distances, NH_3:CH_4 enhancement ratio decreases of at least 20-30% suggest the potential for NH_3 deposition as a loss term for plumes within a few kilometers downwind of feedlots.*** Aircraft boundary layer transect measurements directly above surface mobile measurements in the dairy region show comparable gradients and geometric mean enhancement ratios within measurement uncertainties, even when including NH_3 partitioning to sub-micron particles. Individual NH_3 and CH_4 plumes sampled at close proximity where losses are minimal are not necessarily correlated due to lack of mixing and distinct source pathways. Our analyses have important implications for constraining NH_3 sink and plume variability in-

fluences on regional NH_3 emission estimates and for improving NH_3 emission inventory spatial allocations.

1. Introduction

Atmospheric ammonia (NH_3) is a gas-phase precursor to fine particulate matter ($PM_{2.5}$), contributing to new particle formation and inorganic ammoniated aerosol growth [*Aneja et al.*, 2008; *Pinder et al.*, 2008; *Benson et al.*, 2011]. Anthropogenic NH_3 emissions are increasing predominantly due to agricultural intensification and have important implications for air quality, radiative forcing, and nitrogen deposition to ecosystems downwind of NH_3 source regions [*Galloway et al.*, 2003; *Fenn et al.*, 2010; *IPCC et al.*, 2013]. The San Joaquin Valley (SJV) of California is a region of significant NH_3 emissions due to concentrated animal feeding operations (CAFOs), including dairy feedlots in Tulare County (total ∼500,000 dairy cows), the most productive dairy region in the United States [*CDFA*, 2013]. Excess NH_3 downwind of these sources leads to ammonium nitrate (NH_4NO_3) aerosol formation, which dominates $PM_{2.5}$ mass composition in SJV and contributes to $PM_{2.5}$ concentrations routinely exceeding the U.S. EPA National Ambient Air Quality Standards (NAAQS), especially during stagnant winter conditions [*Watson and Chow*, 2002; *Neuman et al.*, 2003; *SJVAQPCD*, 2012].

Agricultural NH_3 emission source magnitudes and distributions are highly variable and subject to large uncertainties [*Aneja et al.*, 2008; *Beusen et al.*, 2008; *Reis et al.*, 2009; *Sutton et al.*, 2013]. Chemical transport model simulations significantly underestimate gas-phase NH_3 concentrations in SJV compared with satellite and aircraft observations [*Walker et al.*, 2012; *Heald et al.*, 2012; *Kelly et al.*, 2014; *Schiferl et al.*, 2014]. These discrepancies have been linked to NH_3 emission inventory under-estimations and their inability to accurately capture the spatial distributions and temporal trends of feedlot

emissions [*Kelly et al.*, 2014; *Schiferl et al.*, 2014]. Dairy feedlot NH_3 emissions predominantly originate from volatilization of ammonium (NH_4^+) produced by urea hydrolysis in urine and manure deposited onto feedlot surfaces and vary with surface temperatures, wind, soil properties and agricultural practices including dairy housing, feeding methods and manure management [*Beusen et al.*, 2008; *Hristov et al.*, 2011]. These emission controls vary considerably in space and time, challenging ***process-based*** emission modeling approaches [*Pinder et al.*, 2004; *Li et al.*, 2012]. Gas-phase NH_3 also has a short tropospheric lifetime of a few hours to a few days due to aerosol and depositional sinks that vary with ambient temperature, relative humidity, aerosol composition and atmospheric mixing conditions, complicating the interpretation of NH_3 measurements far downwind of sources [*Dragosits et al.*, 2002; *Dennis et al.*, 2010; *Xu and Penner*, 2012]. ***Previous studies modeling NH_3 dry deposition have shown a range of values for the percent of emissions lost via deposition at distances downwind. These include ∼40% loss within 230 m downwind [Hensen et al., 2009], 10.4% loss over the nearest 500 m from the source [Walker et al., 2008] and ∼8-15% dry deposited within a 12 km grid cell in an agricultural region [Dennis et al., 2010]. Dry deposition fluxes are expected to vary across heterogeneous landscapes in agricultural regions and are potentially influenced by bi-directional NH_3 exchange with adjacent cropland or soil surfaces [Bash et al., 2010].***

Ammonia emissions from individual cattle and dairy feedlots have been measured with a variety of in-situ techniques, but these measurements are relatively scarce and limited in characterizing regional emission distributions [*Hristov et al.*, 2011]. There are no routine or widespread NH_3 monitoring networks in SJV [*Clarisse et al.*, 2010] where only

one study has been reported on a single open-lot dairy feedlot [*Cassel et al.*, 2005]. In other regions, flux chambers have been used to quantify emissions at discrete locations within feedlots but have insufficient spatial coverage for sampling spatial heterogeneities on a regional scale [*Mukhtar et al.*, 2008]. Micro-meteorological techniques using point and integrated measurements, including flux gradient [*Griffith and Galle*, 2000; *Cassel et al.*, 2005], relaxed eddy accumulation [*Baum and Ham*, 2009], eddy covariance flux [*Whitehead et al.*, 2008; *Ferrara et al.*, 2012; *Sun et al., accepted*, 2015] and inverse dispersion methods [*Flesch et al.*, 2007; *Griffith et al.*, 2008; *Bjorneberg et al.*, 2009; *Leytem et al.*, 2011, 2013] have been implemented to quantify feedlot NH_3 emissions from daily to seasonal timescales and contributions from different feedlot sections. However, these flux measurements generally do not cover the spatial footprint of many feedlots in an agricultural region, assume flux and wind homogeneities across feedlot sections, and relatively few eddy covariance NH_3 flux measurements have been attempted due to closed-path instrument artifacts that limit response times [*Whitehead et al.*, 2008; *Sintermann et al.*, 2011]. The emission factors derived from these stationary measurements may not be representative of regionally variable NH_3 emissions [*Cassel et al.*, 2005; *Hristov et al.*, 2011]. Mobile measurements with vehicular platforms offer advantages for regional scale emission mapping that expands the spatial coverage of in-situ observations [*Kolb et al.*, 2004; *Brantley et al.*, 2014; *Tao et al.*, 2015]. Recent mobile laboratory observations have quantified emission ratios and apportioned emissions in mixed source regions [*Wang et al.*, 2011; *Pétron et al.*, 2012; *Farrell et al.*, 2013; *Sun et al.*, 2014]. However, previous agricultural plume mobile measurements have been isolated in scope to a single farm or

a two-day survey using a closed-path NH_3 analyzer with limited response time [*Hensen et al.*, 2006, 2009; *Day et al.*, 2012].

Regional scale NH_3 observations offer the potential for characterizing spatio-temporal emission distributions. Satellite NH_3 retrievals, which provide much larger spatial coverage than ground-based observations [*Clarisse et al.*, 2009; *Van Damme et al.*, 2014], have captured surface NH_3 hotspots and regional gradients comparable to in-situ measurements in the SJV at inter-pixel scale [*Clarisse et al.*, 2010; *Shephard and Cady-Pereira*, 2014; *Sun et al.*, 2015], have been compared with models [*Heald et al.*, 2012] and applied for inverse modeling studies constraining U.S. NH_3 emissions [*Zhu et al.*, 2013]. However, satellite NH_3 retrievals are not capable of resolving sub-pixel (single kilometer scale) NH_3 gradients expected for feedlot regions and are limited for detecting diurnal variability with twice daily snapshots for a given location [*Clarisse et al.*, 2010]. Airborne observations are advantageous for boundary layer sampling of NH_3 emission plume distributions relatively close to sources at <1 km spatial resolution [*Nowak et al.*, 2012; *Kelly et al.*, 2014]. Top-down aircraft-based mass balance approaches have been used to estimate regional agricultural emissions of NH_3 [*Nowak et al.*, 2012] and methane (CH_4) [*Wratt et al.*, 2001; *Peischl et al.*, 2012]. However, these flux estimates are limited to optimal wind and boundary-layer condition periods during limited duration field campaigns [*Cambaliza et al.*, 2014] and cannot easily apportion mixed sources within the sampling domain. It is unclear if basin-wide measurements significantly downwind of individual sources are representative of NH_3 emissions with rapid (minutes to hours) and spatially heterogeneous depositional and aerosol NH_3 sinks. Emission ratio approaches are potentially advantageous for quantifying regional agricultural emission signatures relative to other tracers

120 [*Gentner et al.*, 2014]. However, NH_3 emission plume correlations with respect to other
121 emission tracers originating from spatially heterogeneous, distinct source pathways on
122 feedlots have not been investigated. It is currently unknown the extent to which regional
123 observations of NH_3 and other feedlot source tracers can accurately represent agricultural
124 NH_3 emission distributions in regions with spatially heterogeneous NH_3 sources and sinks.
125 No previous studies have investigated agricultural NH_3 emission plume variability with
126 extensive spatial coverage measurements capable of resolving individual feedlot scales.

127 To address these uncertainties, we characterize the spatial distributions of dairy emission
128 plumes in Tulare County from individual feedlot to regional scales with high resolution,
129 surface mobile trace gas measurements during the NASA DISCOVER-AQ California field
130 campaign. We evaluate the statistical significance of linear correlations between NH_3 and
131 CH_4 and characterize spatial emission heterogeneities within a dairy feedlot. We quantify
132 the distributions of NH_3 and CH_4 enhancement ratios in 69 dairy feedlot plumes. We com-
133 pare regional and individual surface plume gradients and enhancement ratios using aircraft
134 and surface mobile observations over similar spatial and temporal domains. Our high res-
135 olution, individual emission plume observations have implications for improving regional
136 scale agricultural NH_3 emission estimates with respect to spatially heterogeneous NH_3
137 losses in the near field region and spatially distinct agricultural tracer emission plumes,
138 as well as improving spatial allocations of feedlot sources in NH_3 emission inventories.

2. Methodology

2.1. Mobile platform measurements

139 Mobile measurements of NH_3, CH_4, carbon dioxide (CO_2), nitrous oxide (N_2O), car-
140 bon monoxide (CO) and water vapor (H_2O) were performed with four open-path sensors

mounted on a typical sedan passenger car (Chevy Impala). This mobile platform is described in detail by *Tao et al.* [2015] and has been used for on-road vehicle emission measurements [*Sun et al.*, 2014]; we briefly describe the platform here. The mobile platform sensor specifications are shown in Table 1. Ammonia, N_2O and CO were measured with two open-path, quantum cascade laser-based sensors employing wavelength modulation absorption spectroscopy (WMS) at 9.06 μm and 4.54 μm respectively [*Tao et al.*, 2012; *Miller et al.*, 2014]. Commercial, open-path analyzers were used for CH_4 (LICOR LI-7700) [*McDermitt et al.*, 2011] and CO_2 (LICOR LI-7500 CO_2/H_2O) measurements. Meteorological parameters (temperature, pressure, relative humidity) were measured with a portable weather station (Vaisala WXT520). Geolocation, vehicle speed, and driving direction were recorded with a GPS unit (GlobalSat EM-406a). Off-line NH_3 calibration was also performed between field measurements based on direct absorption spectroscopy described by *Miller et al.* [2014]. ***A typical calibration curve up to 5 ppmv NH_3 for the present dataset is shown in Figure 4 of Miller et al. [2014], including third-order polynomial fitting for retrievals that do not scale linearly above 100 ppbv NH_3. The calibration curves obtained throughout the mobile platform field campaign generally vary within $\pm$10% [Tao et al., 2015].*** An in-line ethylene reference cell signal was probed continuously to account for NH_3 sensor drift and provided real-time calibration to within $\pm$20% accuracy for NH_3 [*Sun et al.*, 2013]. Although off-line calibration improved the accuracy to $\pm$10%, the field data are reported with $\pm$20% uncertainty to account for drift between off-line calibrations. Nitrous oxide and CO measurements were calibrated similarly using direct absorption and a NOAA GMD standard (325.81 ppbv N_2O with 1 σ of 0.15 ppbv N_2O; 138.5 ppbv CO

±0.7%). Since the N_2O/CO sensor was not operating at the optimal performance level during these measurements, we report data with accuracies of ∼3 ppbv N_2O and ∼5 ppbv CO. Methane measurements were calibrated with a NOAA GMD calibration standard (1872.4±0.3 ppbv CH_4, 3 ppbv uncertainty). Data with insufficient light intensity signals due to rain, dust or insects in the optical path or deposited on the optical cell mirrors were removed (signal intensities below 0.05 V DC (NH_3) and 15% of maximum light intensity (CH_4)). ***The 0.05 VDC cutoff (∼10% of the maximum light intensity values) is applied across the entire dataset and is independent of absolute mixing ratio values. The WMS detection method intrinsically normalizes for small changes in detector signal strength due to alignment that do not correlate with retrieved mixing ratios. However, below the cutoff, the precision starts to degrade significantly (e.g. an order of magnitude worse precision at 0.01 VDC).*** Number densities were corrected for H_2O dilution with H_2O, temperature and pressure measurements to obtain the dry mixing ratios of all species. Raw mixing ratio measurements (0.2 s data) were averaged to 1 s data synchronized to the GPS time stamp. These 1 s time series were synchronized with each other to within 1 s using the cross-correlation method [*Choi et al.*, 2012]. The open-path sensors recorded simultaneous, collocated measurements of these trace gases with fast response times (< 1 s), allowing us to derive enhancement ratios (section 2.3).

2.1.1. Mobile sampling domain

The analyses in this study are based on ground-based mobile measurements performed in Tulare and Kings Counties, California from 28 January to 1 February 2013. The mobile measurement routes in the San Joaquin Valley are shown in Figure 1. Other field

campaign measurement days focused on regions outside the San Joaquin Valley and are not discussed here. Daily measurement durations and conditions are listed in Table 2. The total on-road sampling time in SJV was 31 hours, 19 minutes over a total driving distance of 1053 km. For typical driving speeds of 40-110 km h^{-1}, the spatial resolution of the 1 s mobile measurements is ∼10-30 m. ***The NH_3 and CH_4 measurements retained for the analyses as a percent of all mobile platform data range from 36-86% depending on the sampling day (Table 2) and are generally limited by NH_3 data coverage.*** For the agricultural emission analyses, CO enhancements above background exceeding 500 ppbv were used as the criteria to remove measurements potentially contaminated by combustion-related NH_3 or CH_4 sources, including from our own or nearby vehicles.

2.2. Aircraft measurements

The NASA **D**eriving **I**nformation on **S**urface conditions from **Co**lumn and **Ver**tically Resolved Observations Relevant to **A**ir **Q**uality (DISCOVER-AQ) field campaign took place in the San Joaquin Valley of California during winter 2013 [*NASA*, 2013]. Airborne transects, missed approaches and spirals were conducted by the NASA P3-B aircraft in the Tulare County region during this campaign. Gas-phase NH_3 was measured with a cavity ringdown spectrometer (Picarro G2103) with mixing ratios reported every three seconds, a response time of 8-20 s (80% fall time from 75 ppbv to 20 ppbv NH_3) and total uncertainty of ± (35% + 1.1 ppbv) + 0.34 ppbv NH_3 (1 σ precision) [*NASA Archive*, 2014]. Methane mixing ratios were measured at 1 s time resolution via absorption at 3.3 μm to within 2 ppbv accuracy [*Sachse et al.*, 1991; *NASA Archive*, 2014]. Based on boundary layer P3-B aircraft speeds, the spatial resolution of these NH_3 and CH_4 measurements is 100-300 m

[*NASA Archive*, 2014]. Condensed phase NH_4^+ mass concentrations were measured with Particle-Into-Liquid Sampler/Ion Chromatography (PILS/IC) with 240 s sampling time within 20% accuracy and sensitivity from 30 nm - 1 μm diameter particles [*NASA Archive*, 2014]. PILS/IC NH_4^+ mass concentrations were converted to mixing ratios using observed temperature and pressure. Data from the NASA LaRC airborne High Spectral Resolution Lidar (HSRL) onboard the B-200 aircraft (similar flight locations as P3-B aircraft) were used for estimating planetary boundary layer (PBL) heights (1 minute running means) derived using sharp gradients in aerosol backscatter (532 nm) profiles [*NASA Archive*, 2014; *Scarino et al.*, 2014].

2.2.1. Aircraft sampling domain

We use NASA P3-B aircraft measurements (1 s merged data) on concurrent days with mobile measurement data (30-31 January and 1 February 2013) for the present analyses [*NASA Archive*, 2014]. The P3-B aircraft transects used for the present analyses were performed three times per day directly through the Tulare County region at approximately 300-400 m above ground level (AGL) from Fresno to Bakersfield, California. In the middle of these transects, the aircraft made a missed approach to $\sim$ 30 m AGL at Visalia Municipal Airport.

2.2.2. Wind simulations

The prevailing wind direction is necessary for isolation of downwind measurements. Although the Vaisala weather station measured wind speed and direction, it is biased due to turbulent eddies at the surface and potential effects of the vehicle surface on the free air stream. Previous studies have addressed these large uncertainties when performing analyses with winds measured on a mobile laboratory by implementing mesoscale wind

field simulations [*Johansson et al.*, 2009; *Wang et al.*, 2011]. For hourly mean prevailing wind speed and direction, we used Weather Research and Forecasting (WRF) v3.5 model simulated wind vectors at 10 m above ground level with a spatial resolution of 1.33 km. ECMWF-Interim reanalysis were used to provide initial and boundary conditions and 6 hourly nudging above the boundary layer for WRF. Comparisons with hourly-averaged, ground-level wind observations [*NASA Archive*, 2014] at the Porterville, Visalia, Corcoran and Hanford, California ground sites revealed notably improved simulation of wind direction variability in the 1.33 km domain compared with those in the 4 km domain. Wind simulations at closest grid cell to each ground site generally agree with hourly-averaged ground site wind direction observations. The mean absolute difference (54^o of wind direction) between hourly mean ground site wind directions and mean wind simulations is an upper limit to actual wind simulation biases, as it includes spatial variability of the wind field (local wind shifts) within the modeled grid cell. The sensitivity of plume analyses to these wind direction biases is quantified in section 3.2.1.

2.3. Enhancement ratios

Dairy feedlots emit NH_3 along with a suite of other trace gases such as CH_4, CO_2 and N_2O. However, these species originate from various source pathways (e.g. enteric fermentation and microbial processes in soil/manure) that may not correlate well with NH_3 emission pathways [*Gentner et al.*, 2014; *Owen and Silver*, 2015]. This complicates expressing an NH_3 emission ratio with respect to N_2O, CO_2 or CH_4. N_2O is mainly emitted via microbial processes in soil and manure [*Owen and Silver*, 2015], but ambient N_2O mixing ratio enhancements are very small and rarely detected downwind of most feedlots. CO_2 is emitted by cattle respiration and microbial processes in manure [*Leytem et al.*,

2013], but the urban fossil fuel CO_2 emissions in the measurement domain complicate its use as a unique agricultural emission tracer. For the present analyses, we investigate NH_3 plume correlations with respect to CH_4, a dairy source tracer originating from enteric fermentation and microbial decomposition in managed manure [*Gentner et al.*, 2014; *Owen and Silver*, 2015] that is not easily lost close to the emission source. In addition, very few significant non-agricultural CH_4 sources exist in Tulare County [*Gentner et al.*, 2014]. Although NH_3 and CH_4 emissions originate from different source pathways, both are known to increase with animal activity on feedlots [*van Haarlem et al.*, 2008]. We treat the NH_3:CH_4 ratio as an enhancement ratio, rather than an emission ratio, evaluate its variability and quantify the degree of NH_3 and CH_4 correlations.

Enhancement ratios (ERs) of NH_3 to CH_4 were calculated using the mixing ratios above local background. The time series were separated into a slowly varying background and rapidly changing emission peaks. The background trends were obtained using the 1 percentile over a 400 s moving time window over the 1 s time series, similar to the method used by *Bukowiecki et al.* [2002]. The time window was chosen to be about five times larger than the time scale for cross-wind sampling of a typical NH_3 plume ($\sim$70 s) obtained by the cross-correlation method [*Choi et al.*, 2012] while not too large such that the background would be smoothed and under-estimated. The ER sensitivity to choice of time window is explained in section 3.2.1. Percentile choices less than the 5-percentile impact the ER result by $< 2\%$. Figure 2 illustrates the background trend estimates for a representative mixing ratio time series. The enhancement mixing ratios above background were calculated as $\Delta NH_3 = NH_3$ (measured) - NH_3 (background trend) and similarly for ΔCH_4. The $\Delta NH_3/\Delta CH_4$ enhancement ratios are abbreviated here as

277 NH_3:CH_4. Empirical cutoffs of 4 ppbv ΔNH_3 and 125 ppbv ΔCH_4 were selected to exclude
278 data close to the background levels that may result in negative or spuriously large ER
279 values. ***The empirical cutoffs are not related to the detector light intensity***
280 ***cutoff mentioned above, but data must meet the light intensity cutoff before***
281 ***being considered for ER analysis.*** The ER sensitivity to a factor of two change in
282 empirical cutoff choices is $< 4\%$.

283 Downwind measurements of individual emission plumes were selected based on the wind
284 vectors and sampling distance from dairy feedlots. Feedlot locations were obtained using
285 the California Department of Water Resources land use dataset for Tulare County in
286 2007 (386 dairy feedlots) and Kings County in 2003 (199 dairy feedlots) [*CDWR*, 2007].
287 The mobile platform sampled in the vicinity of 494 dairy farms in these two counties
288 (Figure 1). ***The land cover downwind of most dairy feedlots sampled is field,***
289 ***grain or hay cropland or pasture lands (alfalfa or native vegetation) [CDWR,***
290 ***2007].*** Google Earth imagery from August 2012 was used to verify the locations manually
291 and check for land use changes between 2007 and 2013. Four feedlot locations were
292 updated (added or removed) as appropriate. The WRF simulated horizontal mass flux
293 components at their respective locations were each linearly interpolated to the dairy farm
294 (centroid) locations and were used to compute hourly averaged wind directions at each
295 feedlot location. The maximum sampling distance downwind to select data is explained
296 in section 3.2. The wind vectors in Figure 3a indicate the wind speed and direction during
297 the hour when the mobile platform measured near a given feedlot and all isolated data
298 points are depicted in Figure 3b. The isolation methods verified that the observations
299 used for ERs are primarily representative of dairy emission plumes. We do not expect

petrochemical CH_4 sources to impact the ER results in the Tulare County region since these sources are regionally separated in the San Joaquin Valley [*Gentner et al.*, 2014].

3. Local-scale emission plumes

The mobile platform measured highly variable NH_3 and CH_4 mixing ratios in the Tulare County region that span three orders of magnitude. The NH_3 mixing ratio distribution exhibit distinct hotspots >1 ppmv NH_3 (given by peak heights in Figure 4). Figure S1 shows a closer view of NH_3 mixing ratio variations along one road. Plumes with maxima approaching ∼1 ppmv NH_3 are sampled directly downwind of four feedlots and plumes are not detectable when sampling upwind of other nearby feedlots. In addition, the eastern-most plumes (leftmost in Figure S1) have mixing ratio gradients across the length of one feedlot. Sub-feedlot spatial heterogeneities are investigated further in section 3.1.

We aggregate all enhancement mixing ratios for NH_3 and CH_4 as a function of distance to the closest dairy feedlot edge (Figure 5). Based on a statistical viewpoint across all plumes, extreme maxima (95 percentiles) of ΔNH_3 and ΔCH_4 are typically observed within 100-200 m distance from the dairy feedlots with considerably smaller enhancements observed at longer distances. The maps in Figure 4 and Figure **??** showing localized downwind plumes are consistent with this result. The higher ΔCH_4 values for the data bin at 140 m downwind are due to an extremely high CH_4 enhancement observed downwind of one feedlot, resulting in a mean ΔCH_4 above the 75 percentile of data within this distance bin.

3.1. Spatial heterogeneities within feedlot plumes

Fine scale measurements ($\sim$ 10 m spatial resolution) are applicable to resolve heterogeneities within individual plumes, allowing us to investigate correlations and decay differences between dairy emission tracers. First, we consider a feedlot with distinctly separate sections to investigate correlations and spatial differences with multiple cross wind transects at close proximity. Figure 6 shows a spatial map of NH_3 mixing ratios for three transects ($\sim$23 minutes total sampling time) downwind of one dairy feedlot during evening hours with $\sim$ 1.5 m s^{-1} wind speeds. A dairy corral with cows (section I), fresh manure storage/anaerobic lagoon (section II) and soil/manure piles (section III) are distinctly separate for this feedlot. The mobile measurements captured CH_4 maxima of 80 ppmv downwind of the fresh manure/anaerobic lagoon, N_2O maxima of 600 ppbv downwind of the soil/manure piles, and NH_3 and CO_2 maxima downwind of the dairy corral and soil/manure piles. The high density of data points near the boundary between sections II and III is due to the mobile platform being stopped in that downwind location. ***The mixing ratio profiles of NH_3, CH_4, N_2O and CO_2 downwind of this feedlot are generally consistent and reproducible between three transects over the $\sim$ 23 minute sampling period (Figure 7a). We note that on-road or off-road combustion emissions do not interfere with the gradients observed since there were negligible CO enhancements observed above background during these transects.***

We analyze the correlations and relative enhancements downwind of the three sections to assess the use of enhancement ratios for dairy feedlot plume analyses. ***The sampling distance from each area emission source may be different across the transects,***

so when comparing measurements downwind of different sections we refer to percentage of enhancements rather than percent of total feedlot emissions. The regional backgrounds (assumed to be constant during the transect) are estimated using the minimum mixing ratios observed within the corresponding farm sections. Ammonia and CH_4 are correlated downwind of the dairy corral (r = 0.82) and soil/manure piles (r = 0.68), but poorly correlated downwind of the fresh manure/anaerobic lagoon (r = -0.63) (corresponding scatter plot in Figure S2). ***In addition, N_2O and NH_3 enhancements are collocated downwind of the compost area and moderately correlated (r=0.5), but the NH_3 enhancement closer to the lagoon section is not collocated with an N_2O enhancement. The compost area is likely to have heterogeneously distributed sources of both N_2O (anaerobic conditions for denitrification) and NH_3 (fresh manure with surface urea) across the area of fresh and aged compost piles.***

Based on the integrated area of mixing ratio enhancements across these three sections, ~50% of total feedlot CH_4 enhancements originated from the fresh manure/anaerobic lagoon section, which only comprises ~12% of the feedlot area. In contrast, ~45% of total NH_3 enhancements originated from the dairy corral, with <1% of the NH_3 enhancements downwind of the fresh manure/anaerobic lagoon. ***These results are generally consistent with previous studies where dairy corral surfaces were the dominant NH_3 source [Cassel et al., 2005; Mukhtar et al., 2008] and manure management contributed at least 50% of total CH_4 feedlot emissions for measurements in comparable temperature conditions during our sampling period in the SJV [Leytem et al., 2011; Owen and Silver, 2015]. Finally, all***

NH_3 and CH_4 data points were used to calculate NH_3:CH_4 ratios across the transect and binned by equal number of data points (∼50 m distance per bin) (Figure 7b). Although the geometric mean ER is 0.09 ± 0.02 ppmv ppmv^{-1}, ER values vary by at least an order of magnitude across this feedlot profile (Figure 7b), including between different sections and within single 50 m distance bins.

These observations demonstrate that mobile measurements at close proximity to sources resolve NH_3 and CH_4 plumes from different source pathways not necessarily collocated on a feedlot, making it difficult to interpret the enhancement ratios as true emission ratios on this individual feedlot scale. Most feedlots do not have clearly separated sections. Approximately 66% of Tulare County dairy farms have anaerobic lagoons [*Owen and Silver*, 2015], many of which are located behind the dairy corrals from the perspective of the road sampling locations. These emissions mix with other source plumes during transport across a feedlot area to the mobile measurement locations. Due to the close sampling proximity where these emissions are not well-mixed, we expect to find statistically significant correlation between ΔNH_3 and ΔCH_4 for only a fraction of the plumes sampled.

Ideally, sampling at longer distances downwind where plumes are well-mixed and the entire feedlot is measured as a point source would result in improved correlations and be more advantageous for whole feedlot emission estimates. However, this approach may introduce additional biases due to NH_3 sinks at longer distances downwind. Next, we consider a case of downwind sampling parallel to the wind direction at increasing distance from the source to assess how NH_3 and CH_4 decay relative to each other. Figure 8 depicts this unique case study of an individual feedlot plume sampled approximately parallel to the wind direction on Route 99 in SJV. With no other dairy farm plumes sampled within

5 km downwind, the NH_3 plume is assumed to originate from this one dairy feedlot. The NH_3 and CH_4 plumes extend ∼3.9 km downwind before reaching regional background. Both species are expected to decay similarly if their decay is due to turbulent dispersion only. The NH_3:CH_4 ER decreases by ∼30% from the closest downwind measurements (400 m) to 3 km downwind (Figure 8b). The ER decay indicates the loss of NH_3 relative to the longer-lived CH_4. The PILS/IC NH_4^+ measurements on-board the P3-B aircraft in this region suggest that <15% of NH_3 partitions into the condensed phase. This is a lower limit as the PILS/IC does not sample the entire aerosol size distribution to which NH_3 can be lost. These data suggest that at least 15% of the gas-phase NH_3 emission are lost within the first 3 km downwind due to processes such as NH_3 uptake onto aerosols larger than 1 μm diameter and dry deposition to the surface. For reference, *Dennis et al.* [2010] estimated that 8 - 15% of NH_3 emissions were lost to dry deposition in an agricultural region. Our data suggest there is a significant potential for NH_3 losses, especially for much higher concentration plumes observed in this dataset.

If NH_3 and CH_4 enhancements were originating from the same collocated source, then the ER decay would suggest NH_3 deposition or aerosol sinks. However, non-collocated NH_3 and CH_4 feedlot sources separated by a few hundred meters within the feedlot area could also potentially contribute to the observed ER variability if only one transect is sampled as in this case study. These NH_3 and CH_4 plume intersections are expected to lead to a non-linear decrease in ER with distance downwind. We observed ER variability within the first 1 km downwind due to spatial variations of sources near the feedlot, but the ER decrease is close to linear at distances greater than

1 km downwind. This suggests that the 30% ER decrease is likely due to a combination of NH_3 loss and non-collocated source plumes. To decouple these two effects would require targeted tracer release experiments in this region, which is beyond the scope of the current study.

3.2. Individual plume enhancement ratios

We analyze NH_3:CH_4 ERs in isolated downwind plumes as described in section 2.3. Given that the mobile platform measures only gas-phase NH_3, we must limit the sampling distance to avoid a low ER bias in aged plumes due to NH_3 losses. We find the geometric mean ER decreases by 23% when the sampling distance limit is changed from 1 km to 2 km. The range of spatial sampling was chosen as 1 km from the dairy feedlot centroids to minimize this bias and allow for sufficient sampling size for statistical analysis. This method isolated 69 downwind plumes with collocated mobile NH_3 and CH_4 measurements (Figure 3b).

Due to the close proximity of mobile measurements to feedlot sources, we analyze correlations between NH_3 and CH_4 measurements within the 69 downwind plumes with linear least squares regression. We find 47 downwind plumes (68% of all sampled plumes) had statistically significant linear correlations ($p<0.05$) between ΔNH_3 and ΔCH_4. The lack of correlation in 32% of farm plumes is expected based on the spatially heterogeneous emission signatures described in section 3.1. ***The distribution of sampling distances (up to 1 km downwind) for correlated feedlot plumes has slightly higher mean (138 m) and spans a larger range of distances (95 percentile of 804 m) than the corresponding distances for un-correlated plumes (108 m mean and 435 m 95 percentile), as shown in Figure S3. Therefore, correlated***

plume sampling included longer distances downwind (>500 m), whereas the un-correlated plumes were observed for a shorter sampling distance range (<500 m).

Figure 9 shows the distribution of NH_3:CH_4 values for all data measured within all 69 downwind plumes and within the 47 downwind plumes with statistically significant linear correlations. The median ER for all plumes is 0.14 $\pm$ 0.03 ppmv ppmv^{-1} and the geometric mean is 0.15 $\pm$ 0.03 ppmv ppmv^{-1} ($\pm$ 20% measurement uncertainty, N = 1793). The histogram shows a highly asymmetric distribution (skewness = 5.5) indicative of higher NH_3 emitters relative to CH_4. We use the geometric mean for this positively skewed distribution as it gives smaller weight to the extreme values compared with the arithmetic mean (0.29 ppmv ppmv^{-1}). ***All data points are used in the ER calculations rather than linear regression or area analysis, which underestimate extreme maxima (skewness of 3.0 and 2.0 respectively, based on Figure S4). It is important to note that the histogram (Figure 9) may be an upper limit to actual ER variability due to point by point variations, especially originating from non-collocated source dispersion.*** Measurements within the 47 downwind plumes with statistically significant linear correlations (N=1433) yield a median ER of 0.15 $\pm$ 0.03 ppmv ppmv^{-1} and geometric mean ER of 0.17 $\pm$ 0.03 ppmv ppmv^{-1}, which are 7% and 12% higher than median and geometric mean ERs including all 69 plume measurements. We use all data (not just observations in correlated plumes) for regional aircraft observation comparisons (section 4.3) since regional observations include all plumes with and without statistically significant correlations.

The ER variability across the 69 downwind plumes is illustrated in Figure S5. The order of downwind plumes is arranged according to the order of dairy feedlots in the California Department of Water Resources land use dataset for each day of sampling. We define the relative ER range for each plume as the difference between 5 and 95 percentiles relative to the median ER (expressed in percent). Approximately 77% of plumes have ER variability of at least a factor of two (200% relative range). This relative range is related to how well the plumes have mixed due to distance sampled downwind and wind conditions. It is important to note that the relative range is also a function of the sample size since each plume depicted has a different number of measurements.

3.2.1. Enhancement ratio uncertainties and biases

Enhancement ratio uncertainties and biases originate from multiple factors including concentration measurement uncertainties ($\pm$20% for NH_3 and $\sim$0.1% for CH_4) as well as parameter choices for ER calculations and wind simulations. Sensitivity analyses were performed to quantify potential biases due to background trend fitting parameters. For a time window range from 100 s to 1100 s, the ER sensitivity to changes in time window is $\sim$5%. Sensitivity analyses revealed that shifts of $\pm$ 50^o in wind direction over the entire wind field for a given day resulted in geometric mean ER changes ranging from 22% to <1% depending on the measurement day. A wind direction bias of $\pm$ 50^o over all hours and locations is an extreme case that we do not expect to actually occur. We find that all of these potential biases contribute $\pm$10% uncertainty to ER estimates, which is significantly lower than the relative range of observed ERs (Figure 9b) and within the measurement uncertainties.

4. Regional-scale emission plumes

Next, we characterize regional scale NH_3 and CH_4 plumes using both surface mobile and boundary layer aircraft transects for comparison with the individual plume analyses above.

4.1. Surface regional backgrounds

We analyze the spatio-temporal variability of surface regional background mixing ratios with boundary layer heights (Figure S6). The highest NH_3 and CH_4 mixing ratios were observed during the morning (before 11:00 PST) when PBL heights were <300 m. The lowest mixing ratios occurred during afternoon (12:00 - 17:00 PST) with higher PBL heights (500-800 m altitude), allowing for dilution of surface emissions. For the regional scale analyses, we use the background trends (section 2.3) to eliminate any bias due to non-uniform mobile sampling near large sources. Ammonia and CH_4 background mixing ratio maps were constructed using four days of afternoon measurements (12:00 - 17:00 PST) spatially averaged to 4 km horizontal resolution, which is representative of regional chemical transport model resolutions. Background NH_3 and CH_4 mixing ratios are enhanced in the dairy region (Figure 10b,c), ***denoted by the distribution of land area occupied by dairy feedlots (Figure 10a)***. The maximum NH_3 background (∼35 ppbv) is at least a factor of four above the regional background (<10 ppbv) in the SJV outside of Tulare County. Methane exhibits different spatial patterns and smaller relative mixing ratio enhancements (∼35%) above regional backgrounds compared with NH_3. ***The NH_3 and CH_4 background spatial patterns originate from many factors including gradients in the feedlot spatial densities, emission magnitudes between and within each feedlot at different sampling times***

497 ***on each day, vertical dispersion and horizontal advection from sources, as***
498 ***well as NH_3 sinks. Therefore, the spatial maps qualitatively illustrate NH_3***
499 ***and CH_4 background mixing ratio gradients.***

4.2. Regional plume gradients

500 We compare the regional plume gradients captured by the mobile surface and airborne
501 boundary layer observations. On 31 January 2013, the mobile platform measured along
502 Route 99 within 15 minutes of the midday P3-B aircraft transect almost exactly above the
503 road for $\sim$ 58 km total distance (Figure 11a). The mobile platform and aircraft measure-
504 ments both captured a regional NH_3 plume (>80 ppbv NH_3 enhancement) in the dairy
505 region compared with the surrounding background (< 20 ppbv NH_3) (Figure 11b). Both
506 measurements also captured individual plumes or plume mixtures within the larger re-
507 gional plume, but aircraft measurements with lower (100-300 m) spatial resolution showed
508 lower peak mixing ratios and did not resolve the sharp plumes captured by the mobile
509 surface measurements. The P3-B aircraft also measured plumes shifted southward rela-
510 tive to the surface mobile measurements south of 36.15^o latitude. This shift is indicative
511 of horizontal plume advection due to the prevailing northwest winds as well as vertical
512 dispersion of plumes from the mobile platform location to the aircraft transect altitude.
513 Methane plumes also exhibited similar features, yet their spatial patterns are not iden-
514 tical to those of NH_3, similar to the background spatial maps in Figure 10b,c. Methane
515 enhancements to the south are likely due to petrochemical operations near Bakersfield,
516 California.

4.3. Regional plume enhancement ratios

We derive the regional-scale NH_3:CH_4 ERs from airborne observations for comparison with the individual plume ERs. ***The total sample sizes are N = 1793 (mobile data on 29-31 January and 1 February) and N = 1863 (aircraft data on 30-31 January and 1 February).*** Airborne measurements upwind of the dairy region at the Fresno missed approach are used as a background boundary layer profile and similar empirical cutoffs as for the mobile platform (10 ppbv ΔNH_3 and 100 ppbv ΔCH_4) are selected to exclude data close to the background levels. A correlation plot of NH_3 and CH_4 (not shown) shows a hysteresis effect with a delay in NH_3 enhancement relative to CH_4 when the aircraft entered the regional plume and delay in NH_3 decay when exiting the region due to the response time of the closed-path NH_3 instrument on-board the P3-B aircraft. ***To evaluate the NH_3:CH_4 correlations for matched time responses of both measurements, we convolute the fast response CH_4 measurements with an NH_3 instrument response function using exponential rise and decay time constants based on the 8-20 s NH_3 response time of the Picarro G2103 analyzer for an 80% fall time from 20 to 75 ppbv NH_3 [NASA Archive, 2014]. The correlations between NH_3 and CH_4 airborne transect measurements improved marginally from r = 0.76 to r=0.82 for the afternoon transects with the response function convolution. However, we expect the actual response function to vary with magnitudes of NH_3 concentrations and NH_3 concentration changes throughout the time series. Due to these ambiguities and the marginal improvement in correlations, we do not use a response time correction in the present analyses.*** We do restrict our calculation to the dairy region

only and note that there is only a 3% difference in the geometric mean ER when using all data compared with this restricted domain due to the biases being opposite in sign for entering and exiting the region. We also use only the descending (northern) portion of the missed approach measurements for the ER calculation to avoid the decay artifact for the ascending (southern) portion, evident in (Figure 12b). The domain for ER estimations is also restricted to eliminate the Bakersfield region with significant petrochemical CH_4 sources.

The Visalia missed approach ΔNH_3 and ΔCH_4 vertical profiles during the three transects on 30 January 2013 are shown in Figure 12c and NH_3:CH_4 ER vertical profiles for these transects are illustrated in Figure 13a. The ER values are relatively constant within the $\pm$40% measurement uncertainty from the surface to 300 m altitude in the boundary layer for midday and afternoon transects. No ER values are reported above 200 m altitude for the morning transect due to negligible CH_4 enhancements above the boundary layer with typical morning PBL heights below 300 m AGL (Figure S6).

The geometric mean ER for airborne observations on 30-31 January and 1 February 2013 (0.12 ± 0.05 ppmv ppmv^{-1}) is consistent with individual plume ERs for these days (dotted line in Figure 13b) within the measurement uncertainties. ***The airborne ER observations during afternoon transects were generally reproducible between flight days (Figure 13b) despite differences in temperature ranges and wind directions between these days (Table 2). The individual plume ERs obtained on days with no airborne data (e.g. 28-29 January) were also consistent with the airborne derived ERs.*** However, the surface measurements show much larger extreme values with the 95 percentile a factor of four higher than that for aircraft derived

ERs (Figure 13c). The empirical cutoffs do not significantly influence the 95 percentile values and the geometric mean ER is insensitive to these cutoffs to within 3%. Finally, the geometric mean NH_3:CH_4 ER exhibited an increase in the afternoon (by a factor of four on 30 January 2013) compared with the morning or midday transects (Figure 13a,b) that is clearly driven by higher ΔNH_3 values during the afternoon (Figure 12c).

The impacts of gas-phase NH_3 aerosol partitioning on airborne gas-phase NH_3 measurements is important to evaluate when comparing with close proximity individual plume sampling. We derive ERs with respect to total ammonia ($NH_x = NH_3 + NH_4^+$) using the PILS/IC NH_4^+ measurements onboard the P3-B aircraft. We average the NH_3 airborne data to the 240 s PILS/IC resolution (N=5 data points available in the source region) and add the mixing ratios of NH_3 and NH_4^+ to calculate NH_x. The percent of NH_x measured as NH_4^+ by PILS/IC is $< 15\%$ in the dairy region and $\sim$26% upwind near Fresno. Since NH_4^+ makes up a larger percentage of NH_x upwind than in the source region, ΔNH_x values are comparable to ΔNH_3, implying that the NH_3:CH_4 and NH_x:CH_4 ERs are comparable. Table 3 shows all NH_3:CH_4 and NH_x:CH_4 ER values derived from airborne measurements on 30-31 January and 1 February 2013 within the source region. The percent difference between NH_x:CH_4 and NH_3:CH_4 ranges from -3 to +5% for all data points, significantly below the $\pm$40% ER measurement uncertainty. Although we expect the majority of wintertime NH_4^+ to be found in the accumulation mode (PM_1) in this region [*Herner et al.*, 2006], NH_4NO_3 condensation also occurs on larger particles, a component not included in our NH_x estimate. In addition, NH_x does not account for depositional NH_3 losses.

4.4. Literature comparisons

Emission estimates were compiled from published studies in which winter dairy feedlots emissions of both NH_3 or CH_4 were measured during the same time period at the same feedlot. No such studies have been performed in the Tulare County region. Therefore, we select studies with comparable air temperature conditions and similar open-lot dairy facilities to those found in Tulare County. We calculate the ratios of literature-reported NH_3 and CH_4 emission fluxes (kg d^{-1}) and convert to molar fractions. Table 4 summarizes the present study results and the literature estimates. The literature NH_3:CH_4 ER estimates fall within the distribution of the individual plume ERs derived from our mobile measurements (Figure 13c). As shown in Figure S7, there is a strong seasonal variation in flux ratio as well as variations across the three studies [*Bjorneberg et al.*, 2009; *Leytem et al.*, 2011, 2013]. It is important to note that *Leytem et al.* [2011] and *Leytem et al.* [2013] published January measurements at temperatures 13 - 17^{o}C colder than the minimum temperatures observed during our sampling period in the SJV (Table 2). Therefore, the springtime values with more comparable temperatures to our mobile measurements are reported in Table 4 for these studies.

5. Discussion

5.1. Individual plume measurements

The high spatial resolution, surface mobile observations analyzed in this study are the most extensive spatial survey of NH_3 and CH_4 distributions in an agricultural emission region to date and have revealed significant spatial variability of NH_3 and CH_4 mixing ratios near dairy feedlot sources. NH_3 mixing ratio enhancements alone are not necessarily representative of absolute NH_3 emission variability

as they vary with turbulent dispersion. Absolute emission flux estimates would require Gaussian plume dispersion models for area source regions, which require assumptions on wind, vertical profiles and uniform emission distributions within a feedlot area. In addition, it is difficult to decouple variability of both NH_3 and CH_4 enhancements at individual plume scales due to variable activities and pathways. Activities such as feeding and manure management practices vary considerably between different feedlots [*Hristov et al.*, 2011; *Owen and Silver*, 2015]. Many of these activities, including anaerobic lagoon emissions, are strong functions of temperature, relative humidity and wind conditions [*Sharpe and Harper*, 1999]. Although we expected a lack of correlation between ΔNH_3 and ΔCH_4 due to their known spatially distinct source pathways, the extensive spatial coverage of our individual plume observations allows for a new comprehensive picture of the degree of correlations across an entire source region that impacts enhancement ratio observations on a regional scale.

The mobile measurement dataset obtained over five days is representative of winter daytime conditions in the Tulare and Kings County sampling region. However, given seasonal and diurnal NH_3 and CH_4 emissions variability, this dataset may not representative of nighttime or summer conditions in the same region or much colder winter conditions in other agricultural regions. Since our mobile platform captures each feedlot plume as a snapshot at a different times of the day, the mobile sampling data are not sufficient for characterizing temporal emission trends at individual feedlots. ***Clearly, much more extensive temporal coverage measurements are needed to fully characterize both spatial and temporal variability of feedlot region emissions.***

The NH_3:CH_4 enhancement ratios exhibited decreases of ∼20-30% when sampling 2-3 km downwind. ***This case study highlights the need for more integrated loop and transect measurements around feedlots at multiple downwind distances to integrate across the plume intersections and minimize the influence of non-collocated NH_3 and CH_4 plumes on ER spatial decay.*** Finally, further investigations of dry deposition velocity and bi-directional flux distributions from nearby land surfaces will also be important to constrain NH_3 sinks in high concentration feedlot plumes.

5.2. Regional plume measurements

The spatial gradient comparison shows that the boundary layer aircraft transects and surface mobile measurements captured similar plume mixtures and regional background enhancements. Based on the aircraft transect altitude, both aircraft and mobile platforms sampled individual plumes at similar distances (few hundred meters) to their sources such that minimal NH_3 losses would be expected for these transect observations through the source region. It is remarkable that the geometric mean regional ERs generally agree, within measurement uncertainties, with the individual plume ERs, given there are multiple differences between these ER estimates. Individual plume ERs are derived using background trends while regional enhancements are derived with respect to a background assumed to be constant throughout the source region. Unfortunately, the background trend cannot easily be derived for aircraft data since typical plume widths for aircraft sampling are not easily constrained. Finally, the NH_3:CH_4 ER was consistently larger in the mid-afternoon transect relative to the morning or midday, but this difference is within the measurement uncertainty when comparing the midday and afternoon transects

(Figure 13b). This trend is potentially linked to higher NH_3 surface emissions in the mid-afternoon due to increased solar heating and surface temperatures relative to CH_4 emissions and consistent with other studies of diurnal NH_3 and CH_4 flux measurements [*van Haarlem et al.*, 2008; *Sun et al., accepted*, 2015]. Further investigation is needed to attribute these mechanisms to the observed trends.

6. Summary and implications

We characterized the spatial distributions of winter daytime NH_3 and CH_4 emission plumes in the Tulare County dairy region during the NASA DISCOVER-AQ 2013 field campaign from individual to regional scales. We observed high spatial variability of NH_3 mixing ratios with maxima localized downwind of individual dairy farms and spatially heterogeneous sources within a single feedlot. We quantified for the first time the spatial correlations of NH_3 and CH_4 in 69 individual feedlot plumes and found 68% exhibited statistically significant linear correlation between ΔNH_3 and ΔCH_4. The spatial decay of ERs showed the potential for 20-30% NH_3 losses at several kilometers downwind. These results highlight the tradeoffs between sampling plumes at close proximity compared with longer distances downwind. At close proximities (within 1 km downwind), large and spatially distinct plumes are probed; however, distributed area feedlot source plumes are not well-mixed, resulting in poor correlations between feedlot emission tracers on the local feedlot scale. In contrast, at longer distance sampling, plumes are spatially well-mixed and the feedlot can be seen as a point source; however, NH_3 losses bias measurements several kilometers downwind and mixing of plumes from multiple feedlots can occur.

The regional plume gradient observations from mobile platform and aircraft measurements were comparable, suggesting that regional aircraft transect observations can capture regional gradients also observed at the surface during midday boundary layer conditions in SJV. The surface mobile measurements constrain the nature of individual plume structure at high (10-30 m) spatial resolution, while also capturing the regional background gradient. In contrast, the airborne transect observations are advantageous to capture multiple plume mixtures and sample an entire regional plume multiple times a day at lower resolution (100-300 m). Our airborne and mobile measurement comparisons of spatial gradients and enhancement ratios suggest that NH_3:CH_4 derived using aircraft transects through the source region can be used as an emission ratio in terms of mean or bulk values, although regional observations underestimate and cannot easily distinguish individual feedlot plume variability. When aircraft observations tens of kilometers downwind (rather than transects through the source region as in this study) are used to estimate basin-wide emissions, these analyses must be corrected for potential low biases due to variable NH_3 depositional sinks within the source region.

Mobile NH_3 and other agricultural tracer measurements could be valuable in future investigations to constrain NH_3 dry deposition losses and correct regional enhancement ratio observations. In addition, mobile-based observations are applicable for partitioning different emission pathways in mixed source regions (i.e. petrochemical and agricultural CH_4 emissions) and may be coupled and collocated with open-path eddy covariance flux measurements [*Sun et al., accepted*, 2015], vertically-resolved NH_3 measurements and recently demonstrated thermal infrared hyperspectral imagery techniques [*Tratt et al.*, 2014] to gain a better understanding of NH_3 and CH_4 emission plume structures and

the temporal variability of NH_3 emissions at individual feedlots. Recent studies suggest the potential for improved constraints on CH_4 emissions in California [*Jeong et al.*, 2012; *Wecht et al.*, 2014]. Future efforts to couple CH_4 emission estimates with the geometric mean NH_3:CH_4 are applicable to constrain total mean regional NH_3 emission magnitudes, while individual plume mobile measurements are applicable to improve spatial allocations in NH_3 emission inventories. These observational constraints have significant implications for air quality model predictions of fine aerosol loading downwind of intensive agricultural regions.

Acknowledgments. We acknowledge the support of James Crawford and the DISCOVER-AQ 2013 science team, as well as Trent Proctor (USFS) for providing space for field calibrations in Porterville, California. The authors thank Bruce Anderson for use of the PILS/IC NH_4^+ data and Nathan Trevino (San Joaquin Valley Unified Air Pollution Control District) for use of the ground-based wind observations. All data used in the analyses are publicly available at `http://www-air.larc.nasa.gov/cgi-bin/ArcView/discover-aq.ca-2013` [*NASA Archive*, 2014]. We also thank LICOR Biosciences for use of the LI-7700 methane analyzer and Professor Elie Bou-Zeid for use of the LI-7500 CO_2/H_2O analyzer. We acknowledge logistical assistance and helpful discussions with Da Pan, Paul Ginoux, James Kelly, Joshua DiGangi, Anthony O'Brien, Minghui Diao, Professor James Smith and his research group, and Professor Claire Gmachl and her research group. This research is supported by the NSF Center for Mid-Infrared Technologies for Health and the Environment (MIRTHE, NSF-ERC) under grant no. EEC-0540832. D.J. Miller acknowledges support by the National Science Foundation Graduate Research Fellowship under grant no. DGE-0646086. K. Sun acknowledges support by NASA Earth

and Space Science Fellowship IIP-1263579. The authors acknowledge the support of Hope Michelsen and Ray Bambha for the work on WRF simulations at Sandia National Laboratories that was funded by the Sandia Laboratory Directed Research and Development (LDRD) Program. Sandia is a multiprogram laboratory operated by Sandia Corporation, a Lockheed Martin Company, for the National Nuclear Security Administration under contract DE-AC04-94-AL85000.

References

Aneja, V. P., J. Blunden,, K. James, W.H. Schlesinger, R. Knighton, W. Gilliam, G. Jennings, D. Niyogi, and S. Cole (2008), Ammonia Assessment from Agriculture: U.S. Status and Needs, *J. Environ. Qual.*, *37*, 515–520.

Baum, K. A. and J. M. Ham (2009), Adaptation of a speciation sampling cartridge for measuring ammonia flux from cattle feedlots using relaxed eddy accumulation, *Atmos. Environ.*, *43*, 1753–1759.

Bash, J.O., J.T. Walker, G.G. Katul, M.R. Jones, E. Nemitz and W.P. Robarge, Estimation of In-Canopy Ammonia Sources and Sinks in a Fertilized Zea mays Field (2010), *Env. Sci. and Technol.*, *44* (5), 1683-1689.

Benson, D. R., J. H. Yu, A. Markovich, and S. H. Lee (2011), Ternary homogeneous nucleation of H_2SO_4, NH_3, and H_2O under conditions relevant to the lower troposphere, *Atmos. Chem. Phys.*, *11*, 4755–4766.

Beusen, A. H. W., A. F. Bouwman, P. S. C. Heuberger, G. Van Drecht, and K. W. Van Der Hoek (2008), Bottom-up uncertainty estimates of global ammonia emissions from global agricultural production systems, *Atmos. Environ.*, *42*(24), 6067–6077.

737 Bjorneberg, D. L., A. B. Leytem, D. T. Westermann, P. R. Griffiths, L. Shao, and M. J.
738 Pollard (2009), Measurement of Atmospheric Ammonia, Methane, and Nitrous Oxide
739 at a Concentrated Dairy Production Facility in Southern Idaho Using Open-Path FTIR
740 Spectrometry, *Transactions of the ASABE*, *52*(5), 1749–1756.

741 Brantley, H. L., G. S. W. Hagler, E. S. Kimbrough, R. W. Williams, S. Mukerjee, and L. M.
742 Neas (2014), Mobile air monitoring data-processing strategies and effects on spatial air
743 pollution trends, *Atmos. Meas. Tech.*, *7*, 2169–2183.

744 Bukowiecki, N., Bukowiecki, J. Dommen, A. S. H. Prevot, R. Richter, E. Weingartner,
745 and U. Baltensperger (2002), A mobile pollutant measurement laboratory measuring
746 gas phase and aerosol ambient concentrations with high spatial and temporal resolution,
747 *Atmos. Env.*, *36*, 5569-5579.

748 Cambaliza, M. O. L., P. B. Shepson, D. R. Caulton, B. Stirm, D. Samarov, K. R. Gur-
749 ney, J. Turnbull, K. J. Davis, A. Possolo, A. Karion, C. Sweeney, B. Moser, A. Hen-
750 dricks, T. Lauvaux, K. Mays, J. Whetstone, J. Huang, I. Razlivanov, N. L. Miles, and
751 S. J. Richardson (2014), Assessment of uncertainties of an aircraft-based mass balance
752 approach for quantifying urban greenhouse gas emissions, *Atmos. Chem. Phys.*, *14*,
753 9029–9050.

754 Cassel, T., L. Ashbaugh, D. Meyer and R. Flocchini (2005), Ammonia Flux from Open-
755 Lot Dairies: Development of Measurement Methodology and Emission Factors, *J. Air*
756 *Waste Manag.*, *55*(6), 816–825.

757 CDFA (2013), California Agricultural Statistics Review 2012-2013, California Department
758 of Food and Agriculture.

759 CDWR (2007), California Department of Water Resources, Land Use Data, Available
760 from: http://www.water.ca.gov/landwateruse/lusrvymain.cfm.

761 Choi, W., M. He, V. Barbesant, K. H. Kozawa, S. Mara, A. M. Winer and S. E. Paulson
762 (2012), Prevalence of wide area impacts downwind of freeways under pre-sunrise stable
763 atmospheric conditions, *Atmos. Environ.*, *62*, 318–327.

764 Clarisse, L., C. Clerbaux, F. Dentener, D. Hurtmans, and P. Coheur (2009), Global
765 ammonia distribution derived from infrared satellite observations, *Nat. Geoscience*, *2*,
766 479–483.

767 Clarisse, L., M. W. Shephard, F. Dentener, D. Hurtmans, K. Cady-Pereira, F. Karagu-
768 lian, M. Van Damme, C. Clerbaux, and P.-F. Coheur (2010), Satellite monitoring of
769 ammonia: A case study of the San Joaquin Valley, *J. Geophys. Res.*, *115*, D13302,
770 doi:10.1029/2009JD013291.

771 Day, D. E., X. Chen, K. A. Gebhart, C. M. Carrico, F. M. Schwandner, K. B. Bene-
772 dict, B. A. Schichtrel, and J. L. Collett, Jr. (2012), Spatial and temporal variability of
773 ammonia and other inorganic aerosol species, *Atmos. Environ.*, *61*, 490–498.

774 Dennis, R. L., R. Mathur, J. E. Pleim, and J. T. Walker (2010), Fate of ammonia emissions
775 at the local or regional scale as simulated by the Community Multiscale Air Quality
776 model, *Atmos. Pollut. Res.*, *1*, 207–214.

777 Dragosits, U., M. R. Theobald, C. J. Place, E. Lord, J. Webb, J. Hill, H.M ApSimon, and
778 M. A. Sutton (2002), Ammonia emission, deposition and impact assessment at the field
779 scale: a case study of sub-grid spatial variability, *Environ. Pollut.*, *117*, 147–158.

780 Farrell, P., D. Culling and I. Leifer (2013), Transcontinental methane measurements: Part
781 1. A mobile surface platform for source investigations, *Atmos. Environ.*, *74*, 422–431.

Fenn, M.E., E. B. Allen, S. B. Weiss, S. Jovan, L. H. Geiser, G. S. Tonnesen, R. F. Johnson, L. E. Rao, B. S. Gimeno, F. Yuan, T. Meixner, and A. Bytnerowicz (2010), Nitrogen critical loads and management alternatives for N-impacted ecosystems in California, *J. Environ. Manag.*, *91*, 2404–2423.

Ferrara, R. M. , B. Loubet, P. Di Tommasi, T. Bertolini, V. Magliulo, P. Cellier, W. Eugster, and G. Rana (2012), Eddy covariance measurement of ammonia fluxes: Comparison of high frequency correction methodologies, *Agric. For. Meteorol.*, *158-159*, 30–42.

Flesch, T.K., J. D. Wilson, L. A. Harper, R. W. Todd and N. A. Cole (2007), Determining ammonia emissions from a cattle feedlot with an inverse dispersion technique, *Agricultural and Forest Meteorology*, *144*, 139–155.

Galloway, J. N., J. D. Aber, J. W. Erisman, S. P. Seitzinger, R. W. Howarth, E. B. Cowling, and B. J. Cosby (2003), The Nitrogen Cascade, *BioScience*, *53*, 341–356.

Gentner, D. R., et al. (2014), Emissions of organic carbon and methane from petroleum and dairy operations in California's San Joaquin Valley, *Atmos. Chem. Phys.*, *14*, 4955–4978.

Griffith, D. W. T. and B. Galle (2000), Flux measurements of NH_3, N_2O and CO_2 using dual beam FTIR spectroscopy and the flux gradient technique, *Atmos. Environ.*, *34*, 1087–1098.

Griffith, D. W. T., G. R. Bryant, D. Hsu, and A. R. Reisinger (2008), Methane Emissions from Free-Ranging Cattle: Comparison of Tracer and Integrated Horizontal Flux Techniques, *J. Environ. Qual.*, *37*, 582-591.

Heald, C. L., et al. (2012), Atmospheric ammonia and particulate inorganic nitrogen over the United States, *Atmos. Chem. Phys.*, *12*, 10295–10312.

Hensen, A., T. T. Groot, W. C. M. van den Bulk, A. T. Vermeulen, J. E. Olesen, and K. Schelde (2006), Dairy Farm CH_4 and N_2O Emissions, from One Square Metre to the Full Farm Scale, *Agriculture, Ecosystems and Environment*, *112*, 146–152.

Hensen, A., B. Loubet, J. Mosquera, W. C. M. van den Bulk, J. W. Erisman, U. Dammgen, C. Milford, F. J. Lopmeier, P. Cellier, P. Mikuka, and M. A. Sutton (2009), Estimation of NH_3 emissions from a naturally ventilated livestock farm using local-scale atmospheric dispersion modelling, *Biogeosciences*, *6*, 2847–2860.

Herner, J. D., Q. Ying, J. Aw, O. Gao, D. P. Y. Chang and M. J. Kleeman (2006), Dominant Mechanisms that Shape the Airborne Particle Size and Composition Distribution in Central California, *Aerosol Science and Technology*, *40*(10), 827–844.

Hristov, A. N., M. Hanigan, A. Cole, R. Todd, T. A. McAllister, P. M. Ndegwa, and A. Rotz (2011), Review: Ammonia emissions from dairy farms and beef feedlots, *Canadian Journal of Animal Science*, *91*, 1–35.

IPCC (2013), Climate Change 2013: The Physical Science Basis. Contribution of Working Group I to the Fifth Assessment Report of the Intergovernmental Panel on Climate Change [Stocker, T.F., D. Qin, G.-K. Plattner, M. Tignor, S.K. Allen, J. Boschung, A. Nauels, Y. Xia, V. Bex and P.M. Midgley (eds.)]. Cambridge University Press, Cambridge, United Kingdom and New York, NY, USA, 1535 pp.

Jeong, S., C. Zhao, A. E. Andrews, L. Bianco, J. M. Wilczak, and M. L. Fischer (2012), Seasonal variation of CH_4 emissions from central California, *J. Geophys. Res.*, *117*, D11306, doi:10.1029/2011JD016896.

827 Johansson, M., C. Rivera, B. de Foy, W. Lei, J. Song, Y. Zhang, B. Galle, and L. Molina
828 (2009), Mobile mini-doas measurement of the outflow of NO_2 and HCHO from Mexico
829 city, *Atmos. Chem. Phys.*, *9*, 5647-5653.

830 Kelly, J. T., et al. (2014), Fine-scale simulation of ammonium and nitrate over the South
831 Coast Air Basin and San Joaquin Valley of California during CalNex-2010, *J. Geophys.*
832 *Res. Atmos.*, *119*, doi:10.1002/2013JD021290.

833 Kolb, C. E., S. C. Herndon, J. B. McManus, J. H. Shorter, M. S. Zahniser, D. D. Nelson,
834 J. T. Jayne, M. R. Canagaratna, and D. R. Worsnop (2004), Mobile laboratory with
835 rapid response instruments for real-time measurements of urban and regional trace gas
836 and particulate distributions and emission source characteristics, *Environ. Sci. Technol.*,
837 *38*(21), 5694–5703.

838 Leytem, A. B., R. S. Dungan, D. L. Bjorneberg, and A. C. Koehn (2011), Emis-
839 sions of Ammonia, Methane, Carbon Dioxide, and Nitrous Oxide from Dairy Cat-
840 tle Housing and Manure Management Systems, *J. Environ. Qual.*, *40*, 1383–1394,
841 doi:10.2134/jeq2009.0515.

842 Leytem, A. B., R. S. Dungan, D. L. Bjorneberg, and A. C. Koehn (2013), Greenhouse Gas
843 and Ammonia Emissions from an Open-Freestall Dairy in Southern Idaho, *J. Environ.*
844 *Qual.*, *42*, 10–20.

845 Li, C., W. Salas, R. Zhang, C. Krauter, A. Rotz, and F. Mitloehner (2012), Manure-
846 DNDC: a Biogeochemical Process Model for Quantifying Greenhouse Gas and Ammonia
847 Emissions from Livestock Manure Systems, *Nutrient Cycling in Agroecosystems*, *93*(2),
848 163–200, doi:10.1007/s10705-012-9507-z.

McDermitt, D., G. Burba, L. Xu, T. Anderson, A. Komissarov, B. Riensche, J. Schedlbauer, G. Starr, D. Zona, W. Oechel, S. Oberbauer, and S. Hastings (2011), A new low-power, open-path instrument for measuring methane flux by eddy covariance, *Appl. Phys. B*, *102*, 391–405.

Miller, D.J., K. Sun, L. Tao, M. A. Khan, and M. A. Zondlo (2014), Open-path, quantum cascade-laser-based sensor for high-resolution atmospheric ammonia measurements, *Atmos. Meas. Tech.*, *7*, 81–93, doi:10.5194/amt-7-81-2014.

Mukhtar, S., A. Mutlu, S. C. Capareda, and C. B. Parnell (2008), Seasonal and Spatial Variations of Ammonia Emissions from an Open-Lot Dairy Operation, *J. Air Waste Manag.*, *58*(3), 369–376.

NASA (2013), DISCOVER-AQ — NASA, `http://www.nasa.gov/mission_pages/discover-aq/#.UrNqtfRDvi0`.

NASA Archive (2014), NASA DISCOVER-AQ Data Archive, California 2013. Available at: `http://www-air.larc.nasa.gov/cgi-bin/ArcView/discover-aq.ca-2013`.

Neuman, J. A., et al. (2003), Variability in ammonium nitrate formation and nitric acid depletion with altitude and location over California, *J. Geophys. Res.*, *108*, doi:10.1029/2003JD003616.

Nowak, J. B., J. A. Neuman, R. Bahreini, A. M. Middlebrook, J. S. Holloway, S. A. McKeen, D. D. Parrish, T. B. Ryerson, and M. Trainer (2012), Ammonia sources in the California South Coast Air Basin and their impact on ammonium nitrate formation, *Geophys. Res. Lett.*, *39*, L07804, doi:10.1029/2012GL051197.

Owen, J.J. and Silver, W.L. (2015), Greenhouse gas emissions from dairy manure management: a review of field-based studies, *Global Change Biology*, *21*, 550565, doi:

872 10.1111/gcb.12687.

873 Peischl, J., et al. (2012), Airborne observations of methane emissions from rice cul-
874 tivation in the Sacramento Valley of California, *J. Geophys. Res.*, *117*, D00V25,
875 doi:10.1029/2012JD017994.

876 Pétron, G., et al. (2012), Hydrocarbon emissions characterization in the Colorado Front
877 Range: A pilot study, *J. Geophys. Res.*, *117*, D04304, doi:10.1029/2011JD016360.

878 Pinder, R. W., N. J. Pekney, C. I. Davidson, and P. J. Adams (2004), A process-based
879 model of ammonia emissions from dairy cows: improved temporal and spatial resolution,
880 *Atmos. Environ.*, *38*, 1357–1365.

881 Pinder, R. W., A. B. Gilliland, and R. Dennis (2008), Environmental impact of atmo-
882 spheric NH_3 emissions under present and future conditions in the eastern United States,
883 *Geophy. Res. Lett.*, *35*, doi:10.1029/2008GL033732.

884 Reis, S., R. W. Pinder, M. Zhang, G. Lijie, and M. A. Sutton (2009), Reactive nitrogen
885 in atmospheric emission inventories, *Atmos. Chem. Phys.*, *9*, 7657–7677.

886 Sachse, G. W., J. E. Collins, Jr., G. F. Hill, L. O. Wade, L. G. Burney, and J. A.
887 Ritter (1991), Airborne tunable diode laser sensor for high-precision concentration
888 and flux measurements of carbon monoxide and methane, *SPIE Proceedings 1433*,
889 doi:10.1117/12.46162.

890 Scarino, A. J., et al. (2014), Comparison of Mixed Layer Heights from Airborne High
891 Spectral Resolution Lidar, Ground-based Measurements, and the WRF-Chem Model
892 during CalNex and CARES, *Atmos. Chem. Phys.*, *14*(11), 5547–5560, doi:10.5194/acp-
893 14-5547-2014.

Schiferl, L. D., C. L. Heald, J. B. Nowak, J. S. Holloway, J. A. Neuman, R. Bahreini, I. B. Pollack, T. B. Ryerson, C. Wiedinmyer, and J. G. Murphy (2014), An investigation of ammonia and inorganic particulate matter in California during the CalNex campaign, *J. Geophys. Res. Atmos.*, *119*, 1883-1902, doi:10.1002/2013JD020765.

Sharpe, R.R. and L. A. Harper (1999), Methane emissions from an anaerobic swine lagoon, *Atmos.Environ.*, *33*, 3627–3633.

Shephard, M. W. and K.E. Cady-Pereira (2014), Cross-track Infrared Sounder (CrIS) satellite observations of tropospheric ammonia, *Atmos. Meas. Tech. Discuss.*, *7*, 11379-11413, doi:10.5194/amtd-7-11379-2014.

Sintermann, J., C. Spirig, A. Jordan, U. Kuhn, C. Ammann, and A. Neftel (2011), Eddy covariance flux measurements of ammonia by high temperature chemical ionisation mass spectrometry, *Atmos. Meas. Tech.*, *4*, 599–616, doi10.5194/amt-4-599-2011.

SJVAQPCD (2012), San Joaquin Valley Air Pollution Control District 2012 $PM_{2.5}$ Plan, Available at: `http://www.valleyair.org/Air_Quality_Plans/PM25Plan2012/CompletedPlanbookmarked.pdf`.

Sun, K., L. Tao, D. J. Miller, M. A. Khan, and M. A. Zondlo (2013), In-line Multi-harmonic Calibration Method for Open-path Atmospheric Ammonia Measurements, *Appl. Phys. B*, *110*, 213–222.

Sun, K., L. Tao, D. J. Miller, M. A. Khan, and M. A. Zondlo (2014), On-Road Ammonia Emissions Characterized by Mobile, Open-Path Measurements, *Envir. Sci Technol.*, doi:10.1021/es4047704.

Sun, K., K. Cady-Pereira, D.J. Miller, L. Tao, M.A. Zondlo, J.B. Nowak, J.A. Neuman, T. Mikoviny, M. Mller, A. Wisthaler, A.J. Scarino and C.A. Hostetler (2015), Validation of TES ammonia observations at the single pixel scale in the San Joaquin Valley during DISCOVER-AQ, J. Geophys. Res.-Atmos., 120, doi:10.1002/2014JD022846.

Sutton, M.A., et al. (2013), Towards a climate-dependent paradigm of ammonia emission and deposition, *Philosophical Transactions of the Royal Society of London B: Biological Sciences*, *368*:1621, doi:10.1098/rstb.2013.0166.

Tao, L., K. Sun, M. A. Khan, D. J. Miller, and M. A. Zondlo (2012), Compact and portable open-path sensor for simultaneous measurements of atmospheric N_2O and CO using a quantum cascade laser, *Opt. Express*, *20*, 28106–28118.

Tao, L., K. Sun, D.J. Miller, D. Pan, L.M. Golston and M.A. Zondlo (2015), Low-power, open-path mobile sensing platform for high-resolution measurements of greenhouse gases and air pollutants, Appl. Phys. B, DOI 10.1007/s00340-015-6069-1.

Tratt, D.M., K.N. Buckland, J.L. Hall, P.D. Johnson, E.R. Keim, I. Leifer, K. Westberg and S.J. Young (2014), Airborne visualization and quantification of discrete methane sources in the environment, *Remote Sensing of Environment*, *154*, 74-88.

Van Damme, M., L. Clarisse, C. L. Heald, D. Hurtmans, Y. Ngadi, C. Clerbaux, A. J. Dolman, J. W. Erisman, and P. F. Coheur (2014), Global distributions, time series and error characterization of atmospheric ammonia (NH_3) from IASI satellite observations,

939 *Atmos. Chem. Phys.*, 14(6), 2905-2922, doi:10.5194/acp-14-2905-2014.

940 van Haarlem, R.P., R.L. Desjardins, Z. Gao, T.K. Flesch and X. Li (2008), Methane and
941 ammonia emissions from a beef feedlot in western Canada for a twelve-day period in
942 the fall, *Canadian Journal of Animal Science*, *88*:4, 641-649, 10.4141/CJAS08034.

943 Walker J., P. Spence, S. Kimbrough and W. Robarge (2008), Inferential model estimates
944 of ammonia dry deposition in the vicinity of a swine production facility, *Atmos. Envir.*,
945 *42*:14, 3407-3418.

946 Walker, J. M., S. Philip, R. V. Martin, and J. H. Seinfeld (2012), Simulation of nitrate,
947 sulfate, and ammonium aerosols over the United States, *Atmos. Chem. Phys.*, *12*, 11213–
948 11227, doi10.5194/acp-12-11213-2012.

949 Wang, M., T. Zhu, J. Zhang, Q. Zhang, W. Lin, Y. Li, and Z. Wang (2011), Using a
950 mobile laboratory to characterize the distribution and transport of sulfur dioxide in
951 and around Beijing, *Atmos. Chem. Phys.*, *11*(22), 11631–11645.

952 Watson, J. G. and J. C. Chow (2002), A Wintertime $PM_{2.5}$ Episode at the Fresno, CA,
953 Supersite, *Atmos. Environ.*, *36*, 465–475.

954 Wecht, K. J., D. J. Jacob, M. P. Sulprizio, G. W. Santoni, S. C. Wofsy, R. Parker, H.
955 Bsch, and J. Worden (2014), Spatially resolving methane emissions in California: con-
956 straints from the CalNex aircraft campaign and from present (GOSAT, TES) and future
957 (TROPOMI, geostationary) satellite observations, *Atmos. Chem. Phys.*, *14*, 8173–8184,
958 doi:10.5194/acp-14-8173-2014.

959 Whitehead, J. D., M. Twigg, D. Famulari, E. Nemitz, M. A. Sutton, M. W. Gallagher, and
960 D. Fowler (2008), Evaluation of Laser Absorption Spectroscopic Techniques for Eddy
961 Covariance Flux Measurements of Ammonia, *Environ. Sci. Technol.*, *42*, 2041–2046.

962 Wratt, D. S., N. R. Gimson, G. W. Brailsford, K. R. Lassey, A. M. Bromley, and M. J.
963 Bell (2001), Estimating regional methane emissions from agriculture using aircraft mea-
964 surements of concentration profiles, *Atmos. Environ.*, *35*, 497–508.

965 Xu, L. and J. Penner (2012), Global simulations of nitrate and ammonium aerosols and
966 their radiative effects, *Atmos. Chem. Phys.*, *12*(20), 9479–9504.

967 Zhu, L., D. K. Henze, K. E. Cady-Pereira, M. W. Shephard, M. Luo, R. W. Pinder, J. O.
968 Bash, and G.-R. Jeong (2013), Constraining U.S. ammonia emissions using TES remote
969 sensing observations and the GEOS-Chem adjoint model, *J. Geophys. Res. Atmos.*, *118*,
970 3355-3368, doi:10.1002/jgrd.50166.

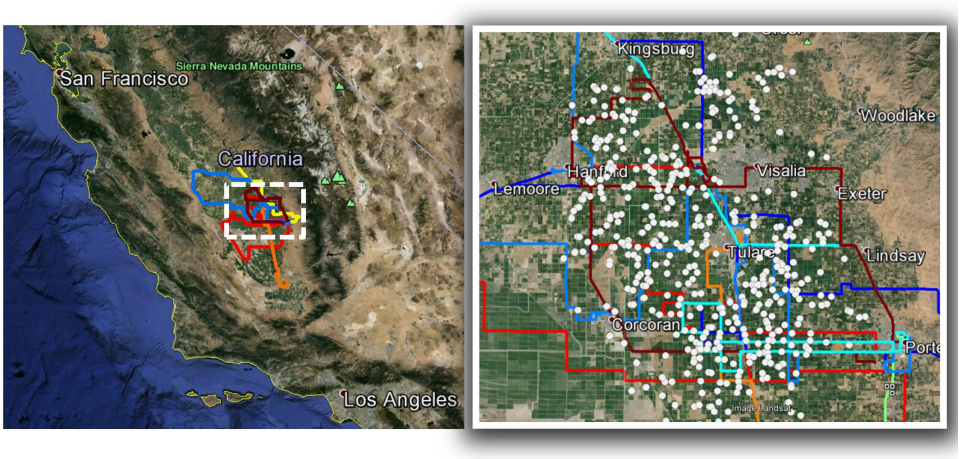

Figure 1. Mobile measurement routes during the NASA DISCOVER-AQ 2013 field campaign in the Tulare County region of the San Joaquin Valley, California. The colors represent the routes covered on each day in the San Joaquin Valley. The map at right shows the region indicated by the dotted square at left with the white points denoting locations of dairy feedlots (California Department of Water Resources Land use data set).

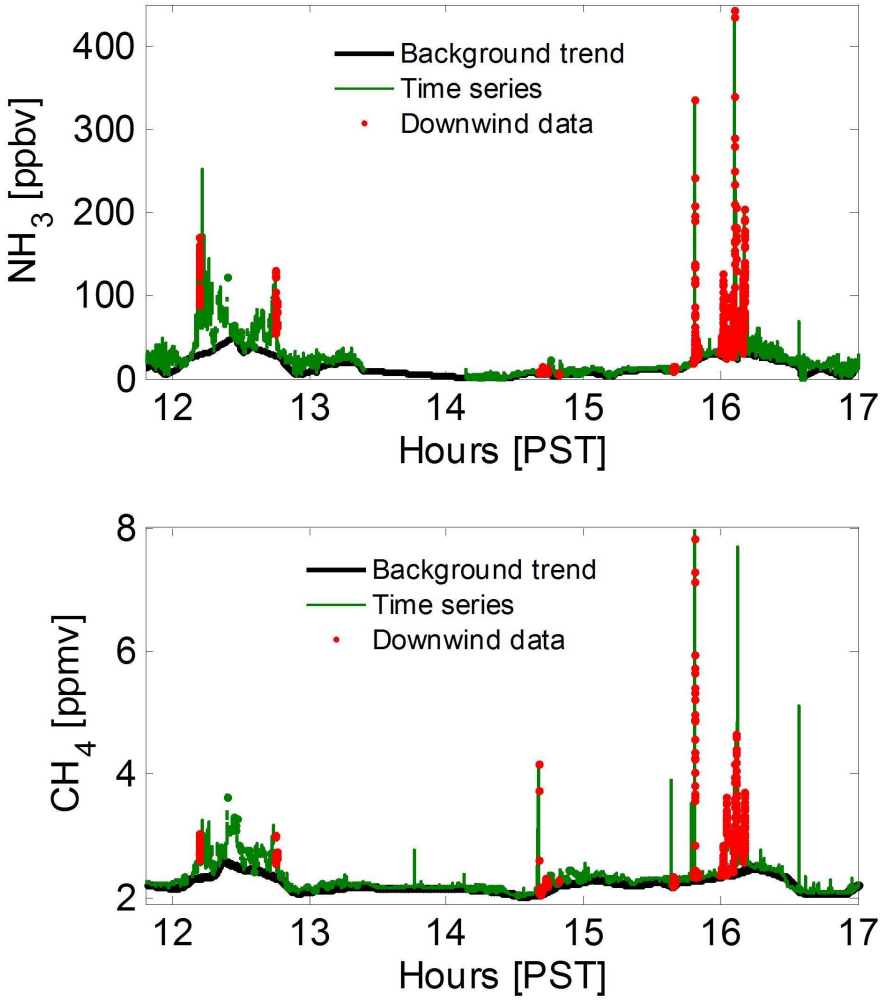

Figure 2. Representative time series of mobile NH_3 and CH_4 measurements (green), along with background trend fitting (black) and data points selected downwind of dairy farms (red).

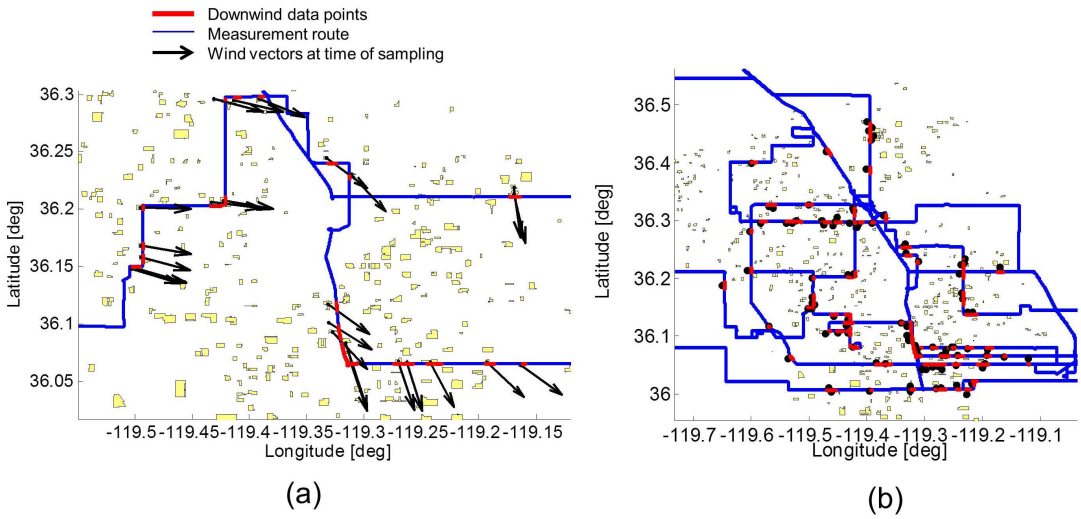

Figure 3. (a) Map of mobile measurement route on February 1, 2013 depicting downwind data point isolation. The mobile measurement route (blue), dairy feedlot polygons (yellow) and wind vectors (black) at the time of passing a given dairy feedlot are indicated; (b) The corresponding map, as in (a), for the entire sampling region over four days (29 January 29 to 1 February 2013).

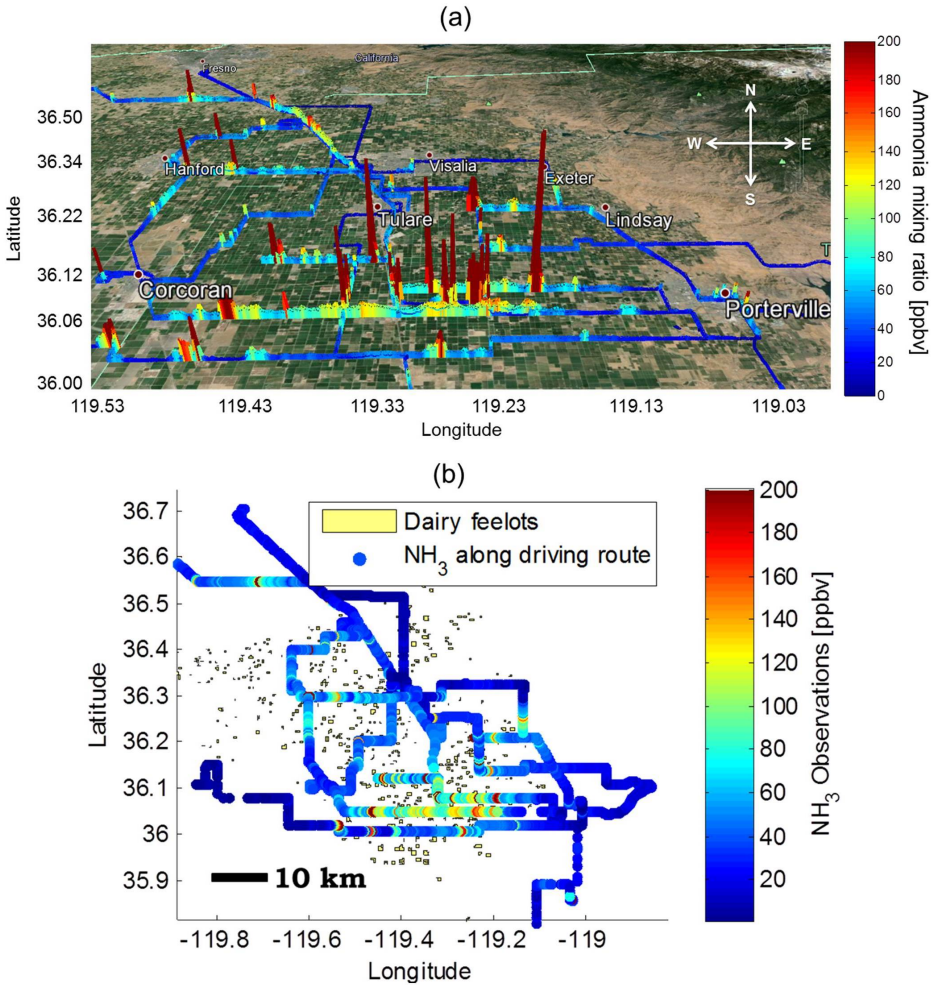

Figure 4. (a) Mobile spatial measurements of NH_3 mixing ratios (5 s averages of 1 s data for optimal display) on Google Earth imagery of the Tulare County region on 28 January 28 to 1 February 2013. The mixing ratios above the color scale are denoted by the peak heights and reach up to 1 ppmv NH_3. (b) The same dataset as depicted in (a) with locations of dairy feedlot facilities (yellow polygons with black outlines).

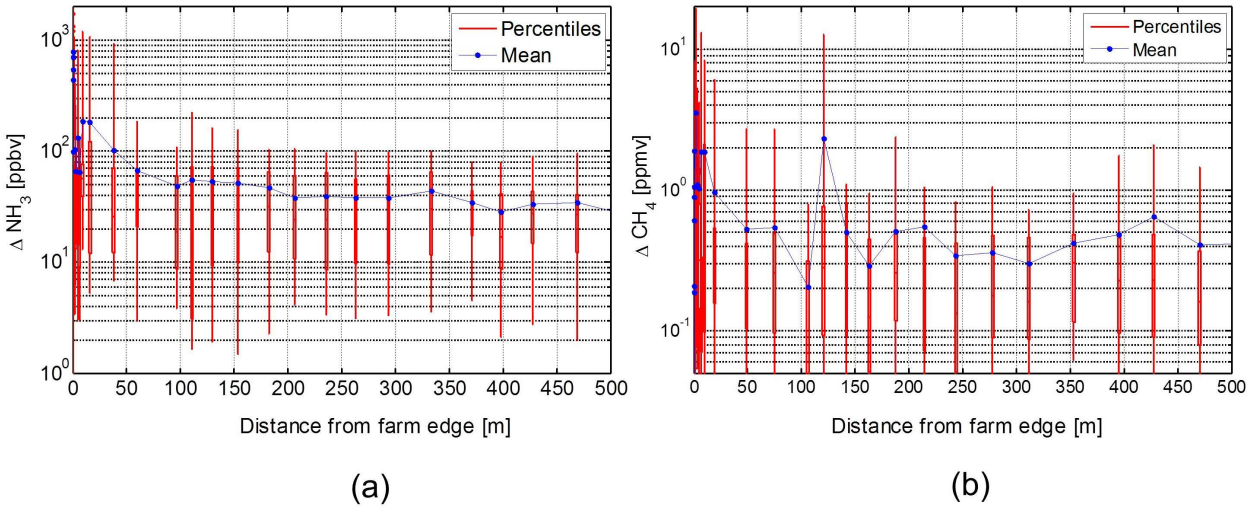

Figure 5. Box-whisker plots of (a) ΔNH_3 and (b) ΔCH_4 as a function of distance downwind of the closest dairy feedlot edge. The plot is binned by equal number of data points sampled at a given distance. The bins are clustered at distances near zero due to the large number of data points at close proximity. ***The log-linear scale better illustrates the variations at farther sampling distances***

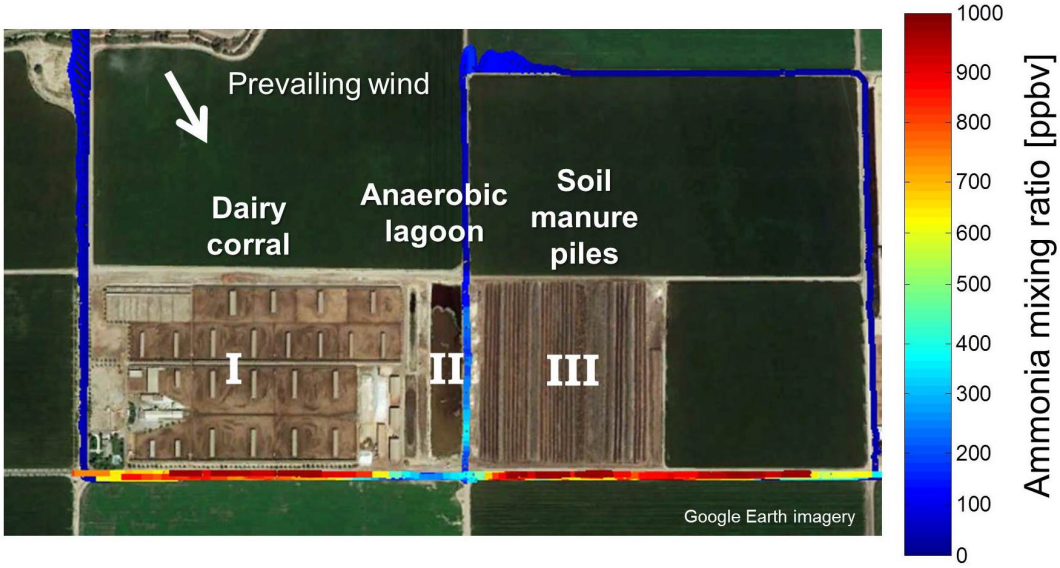

Figure 6. Ammonia mixing ratio spatial measurements during the evening of 29 January 2013 at one dairy feedlot in Tulare County (with Google Earth imagery). The arrow indicates the prevailing (northwest) wind direction and distinct sections are as follows: (I) dairy corrals, (II) fresh manure storage/anaerobic lagoon and (III) soil/manure piles. The length of the farm (left to right) is $\sim$ 1600 m.

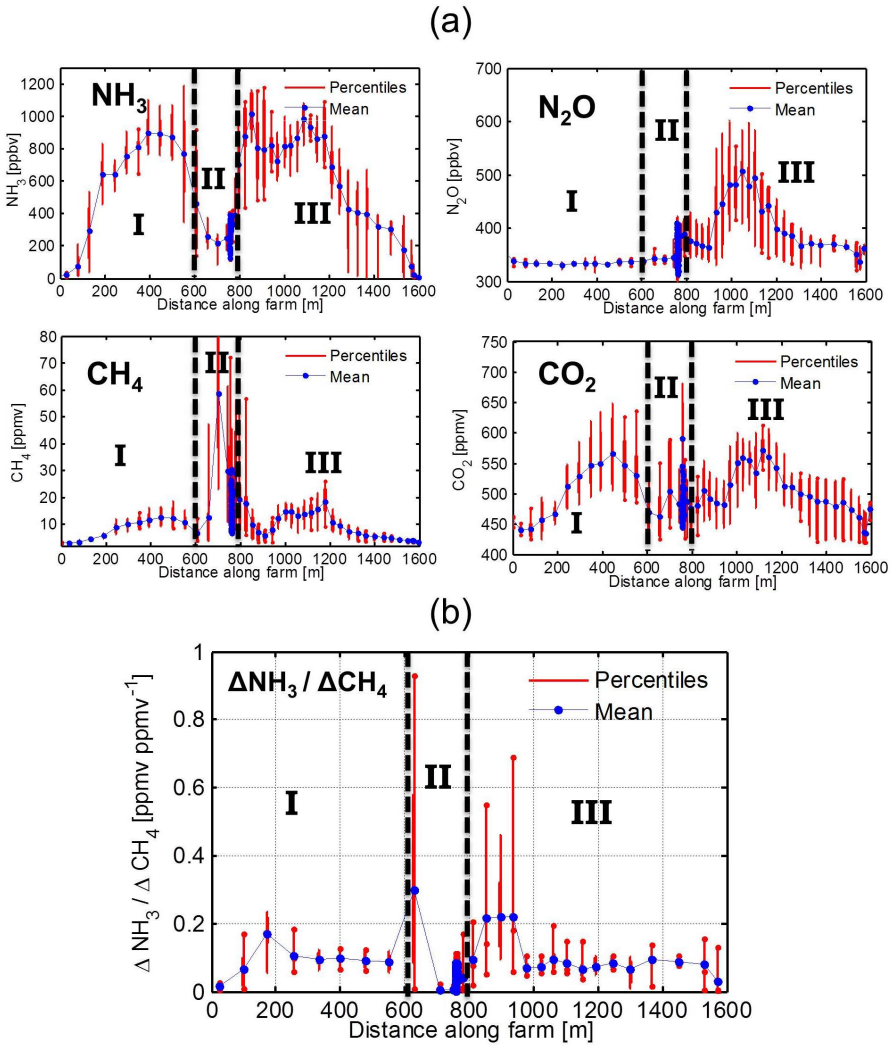

Figure 7. (a) Spatial distributions of NH_3, CH_4, N_2O and CO_2 mixing ratios along the downwind edge of one dairy feedlot for 2-3 transects over $\sim$ 23 minutes. The sections defined in Figure 6 are labeled in the time series (I, II, III). The red lines denote the 5 and 95 percentiles within each bin of equal number of data points. (b) $\Delta NH_3/\Delta CH_4$ enhancement ratio percentiles and arithmetic means across the three feedlot sections.

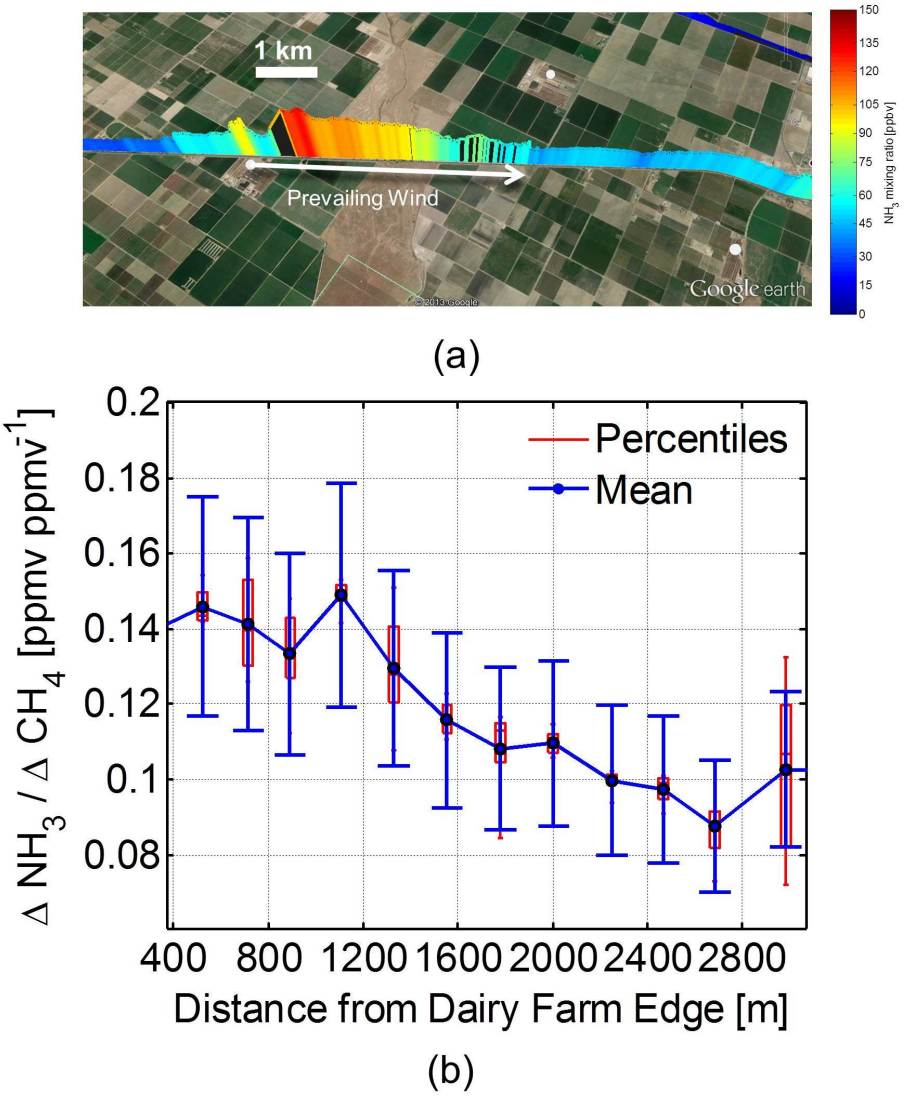

Figure 8. (a) Ammonia mixing ratios (1 s data) measured along one dairy feedlot plume on 31 January 2013 (12:43 PST). The measurement route (Route 99) is approximately parallel to the wind direction (arrow). (b) $\Delta NH_3/\Delta CH_4$ enhancement ratios for the plume in (a), as a function of distance downwind of the dairy feedlot source. The error bars indicate the measurement uncertainty ($\pm$ 20%) and the red box-whiskers indicate the variability of measurements for data in each distance bin.

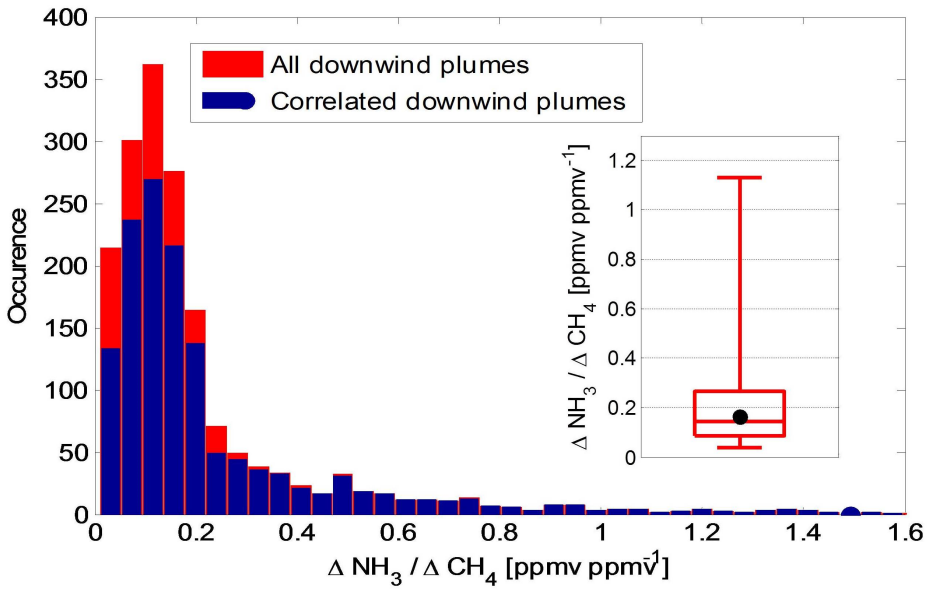

Figure 9. Histogram of the NH_3:CH_4 enhancement ratio distribution for all isolated downwind plume measurements (red) and plume measurements with statistically significant correlations between NH_3 and CH_4 enhancements (blue). Inset: box-whisker plot of the ER percentiles and geometric mean (black point) for all downwind plumes.

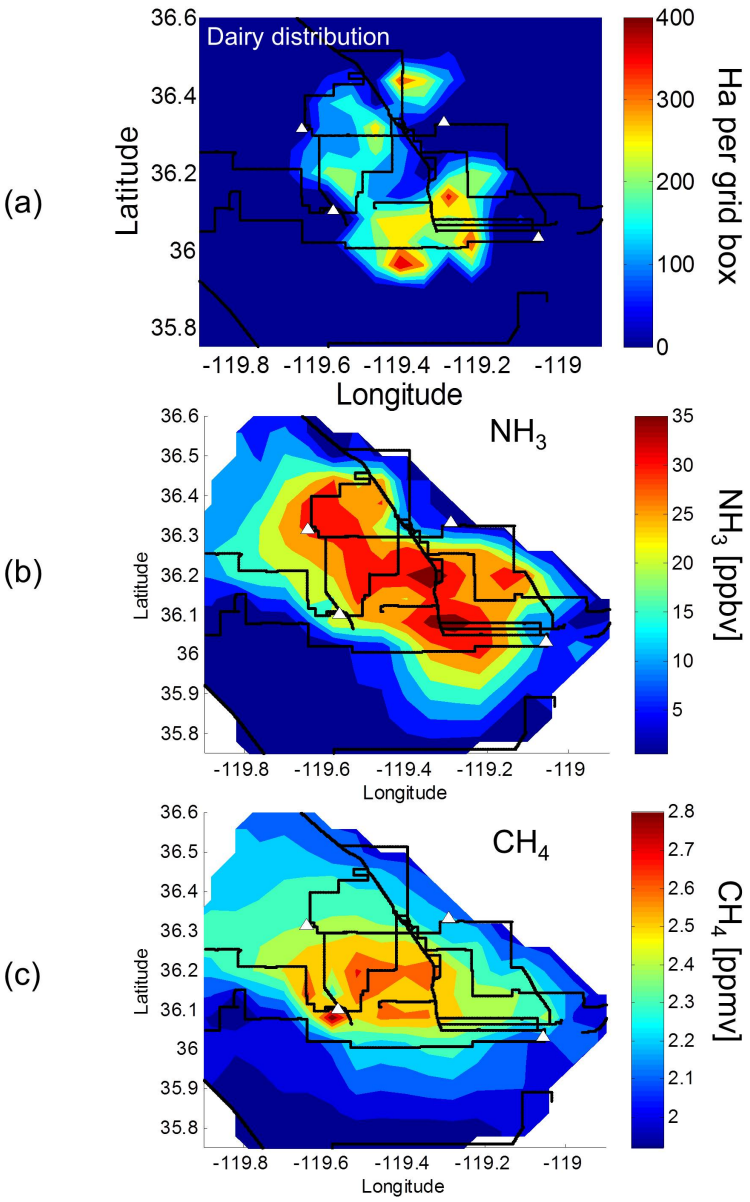

Figure 10. (a) Dairy distributions expressed as the total dairy feedlot area (Ha) per 4 km resolution grid cell (California Water Resources Landuse Dataset) with linear interpolation. (b) Spatial maps of NH_3 and CH_4 background mixing ratios for measurements performed between 12:00 - 17:00 PST on 29 January to 1 February 2013. The data are spatially averaged on the same 4 km grid and linearly interpolated as in (a). The black lines denote the locations of mobile measurements. The white triangles denote the locations of Visalia, Porterville, Corcoran and Hanford, California (clockwise from upper right triangle) as reference locations.

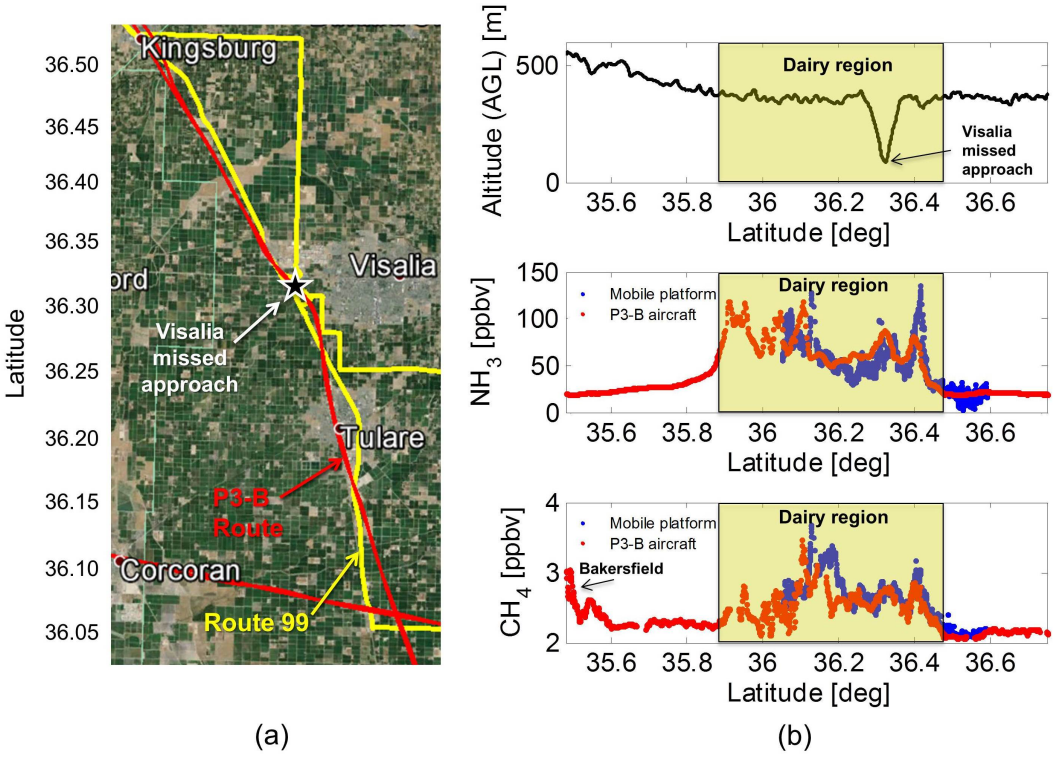

Figure 11. (a) Mobile platform routes (yellow) from 12:15-13:00 PST and NASA P3-B aircraft transect (red) from 12:45-13:10 PST on 31 January 2013. The Visalia Municipal airport missed approach location is indicated by the star symbol. (b) NASA P3-B altitude (top plot), NH_3 and CH_4 mixing ratios (middle and bottom plots) as a function of latitude measured by the mobile platform and on-board the P3-B aircraft for the transects described in (a). The shaded regions indicate the dairy region (based on the latitudes with non-zero dairy densities in Figure 13a). The Bakersfield region is labeled for reference.

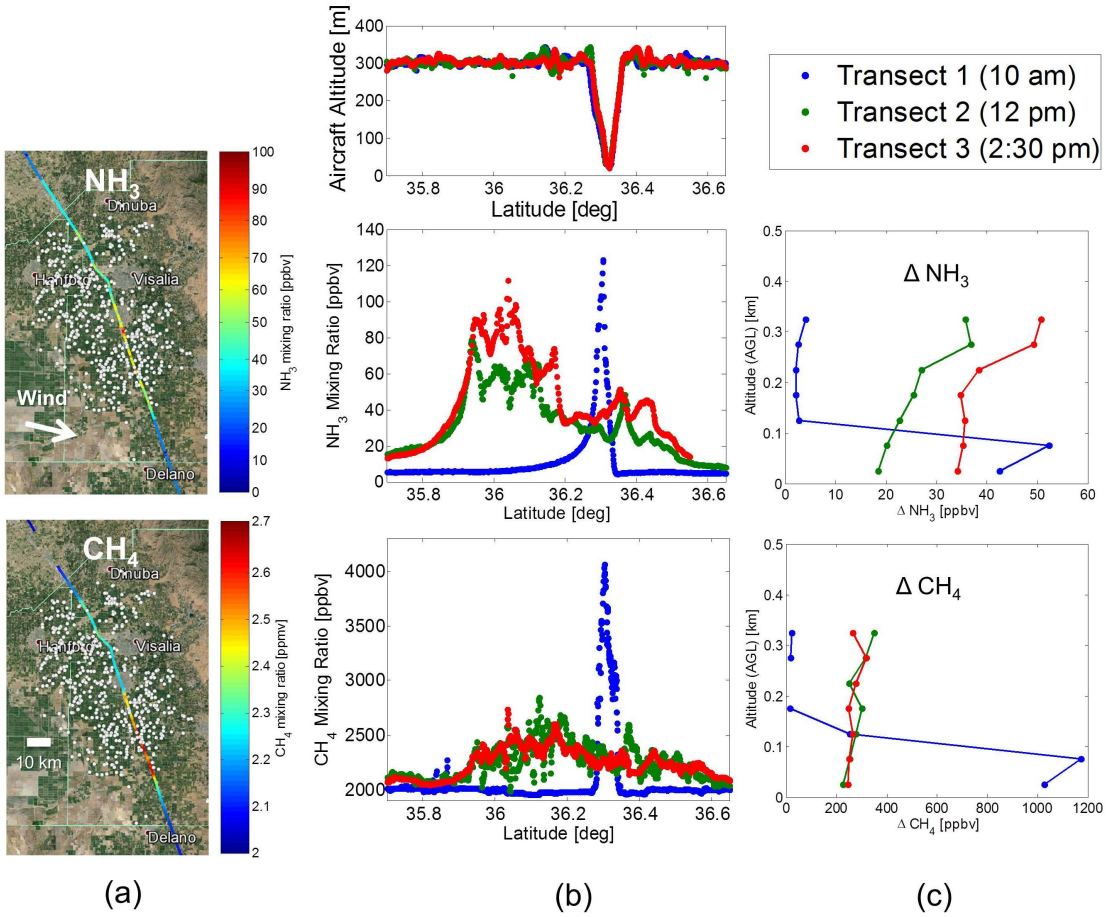

Figure 12. (a) NASA P3-B aircraft 12:00 PST transect NH_3 and CH_4 observations from Fresno to Bakersfield, California on 30 January 2013. Wind direction and distance scales are indicated and white points denote dairy feedlot locations (California Department of Water Resources). (b) Latitudinal gradients of aircraft altitude (AGL), NH_3 and CH_4 mixing ratios for the transect shown in (a). (c) Vertical distributions of ΔNH_3 and ΔCH_4 (arithmetic means within 50 m vertical bins).

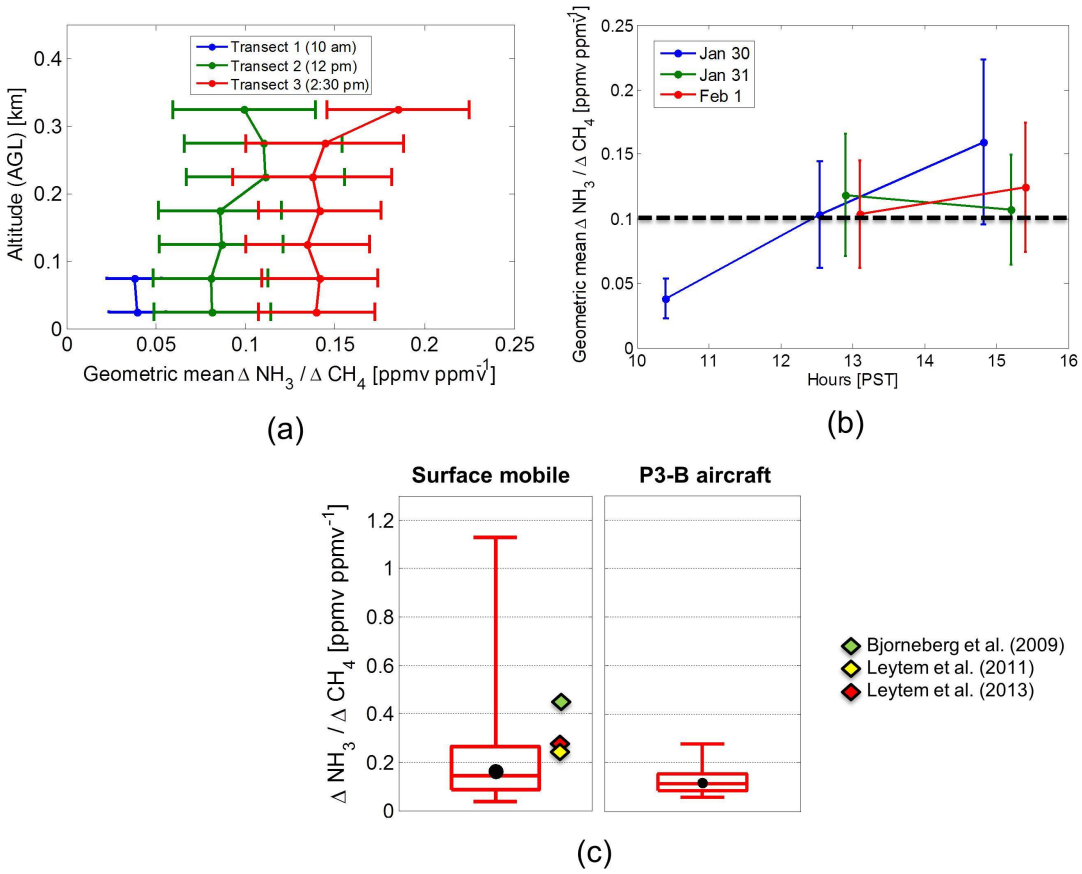

Figure 13. (a) NH_3:CH_4 vertical distributions for all transects on 30 January 2013, displayed as the geometric means within 50 m vertical bins. The error bars indicate the measurement uncertainty (± 40%). (b) Geometric mean NH_3:CH_4 ERs during P3-B aircraft transects on 30-31 January and 1 February 2013. The error bars represent the measurement uncertainties (± 40%). No morning transects were flown on 31 January or 1 February. The dotted line represents the geometric mean NH_3:CH_4 ER for mobile surface measurements on the corresponding flight days. (c) Percentiles and geometric mean ERs derived from surface mobile (left) and aircraft measurements (right). The literature study ERs shown in Table 4 are indicated by the colored diamonds.

Table 1. Summary of the open-path mobile platform sensor specifications, metrics and references containing further details.

Species	**Precision**	**Mass**	**Power**	**References**
NH_3	0.15 ppbv	15 kg	50 W	Miller et al. (2014)
N_2O	0.07 ppbv	10 kg	40 W	Tao et al. (2012)
CO	0.2 ppbv	-	-	Tao et al. (2012)
CH_4	2 ppbv	5.2 kg	8 W	LICOR (McDermitt et al., 2011)
CO_2	0.1 ppmv	0.75 kg	12 W	LICOR
H_2O	$< 1\%$	-	-	LICOR
T,P,RH	-	-	-	Vaisala

Table 2. San Joaquin Valley on-road measurement conditions and durations used in this study.

Days in 2013	**Start time (PST)**	**End time (PST)**	**Driving distance (km)**	**Air temperature (°C)**	**Wind direction**	**ER; data coverage (**
28 January	13:23	16:10	129	11-13	WSW	71
29 January	10:45	19:21	306	9-16	SW - NW	36
30 January	10:59	17:10	164	12-18	SW - W	86
31 January	11:21	17:18	185	15-20	NW	83
1 February	8:58	16:46	269	11-19	NW	48

Table 3. Comparison of airborne $\Delta NH_3/\Delta CH_4$ and $\Delta NH_x/\Delta CH_4$ ERs.

Date	**Transect No.**	$\mathbf{\Delta NH_3/\Delta CH_4}$	$\mathbf{\Delta NH_x/\Delta CH_4}$	**Percent Change using $\mathbf{NH_x}$ [%]**
30-Jan	2	0.0804	0.0803	-3
30-Jan	3	0.147	0.149	+1
30-Jan	3	0.197	0.192	-3
31-Jan	3	0.130	0.137	+5
1-Feb	3	0.174	0.176	+1

Table 4. Comparison of mobile platform observations with molar dairy emission flux ratios from relevant case studies in the published literature.

Published Emissions	**NH_3:CH_4 [ppmv ppmv^{-1} or mol mol^{-1}]**	**Air Temperature Range [^{o}C]**
Current study (mobile) median	0.14 ± 0.03	9-20
Current study (mobile) geometric mean	0.15 ± 0.03	9-20
Bjorneberg et al. (2009)	0.45	-1 - 16
Leytem et al. (2011)	0.24	8 - 14
Leytem et al. (2013)	0.25	8 - 13